3

PASSIVE DENDRITIC TREES

The previous chapter dealt with the solution of the cable equation in response to current pulses and steps within a single unbranched cable. However, real nerve cells possess highly branched and extended dendritic trees with quite distinct morphologies. Figure 3.1 illustrates the fantastic variety of dendritic trees found throughout the animal kingdom, ranging from neurons in the locust to human brain cells and cells from many different parts of the nervous system. Some of these cells are spatially compact, such as retinal amacrine cells, which are barely one-fifth of a millimeter across (Fig. 3.1E), while some cells have immense dendritic trees, such as α motoneurones in the spinal cord extending across several millimeters (Fig. 3.1A). Yet, in all cases, neurons are very tightly packed: in vertebrates, peak density appears to be reached in the granule cell layer of the human cerebellum with around 5 million cells per cubic millimeter (Braitenberg and Atwood, 1958) while the packing density of the cells filling the 0.25 mm^3 nervous system of the housefly *Musca domestica* is around 1.2 million cells per cubic millimeter (Strausfeld, 1976). The dendritic arbor of some cell types encompasses a spherical volume, such as for thalamic relay cells (Fig. 3.1G), while other cells, such as the cerebellar Purkinje cell (Fig. 3.1F and K), fill a thin slablike volume with a width less than one-tenth of their extent.

Different cell types do not appear at random in the brain but are unique to specific parts of the brain. By far the majority of excitatory cells in the cortex are the *pyramidal cells* (Fig. 3.1C). Yet even within this class, considerable diversity exists. But why this diversity of shapes? To what extent do these quite distinct dendritic architectures reflect differences in their roles in information processing and computation? What influence does the dendritic morphology have on the electrical properties of the cell, or, in other words, what is the relationship between the morphological structure of a cell and its electrical function?

One of the few cases where a quantitative relationship between form and some aspect of neuronal function has been established is the retinal neurons. It seems obvious that the larger their dendritic tree, the larger the visual area over which they can receive input.[1] That this is true for large cells was shown by Peichl and Wässle (1983). They correlated the electrophysiologically defined receptive field of one type of retinal ganglion cell (*brisk transient* or Y cell) with its dendritic tree size. It is well known that the physiologically

1. The area in visual space in which an appropriate visual input will excite a cell is termed its *classical receptive field.*

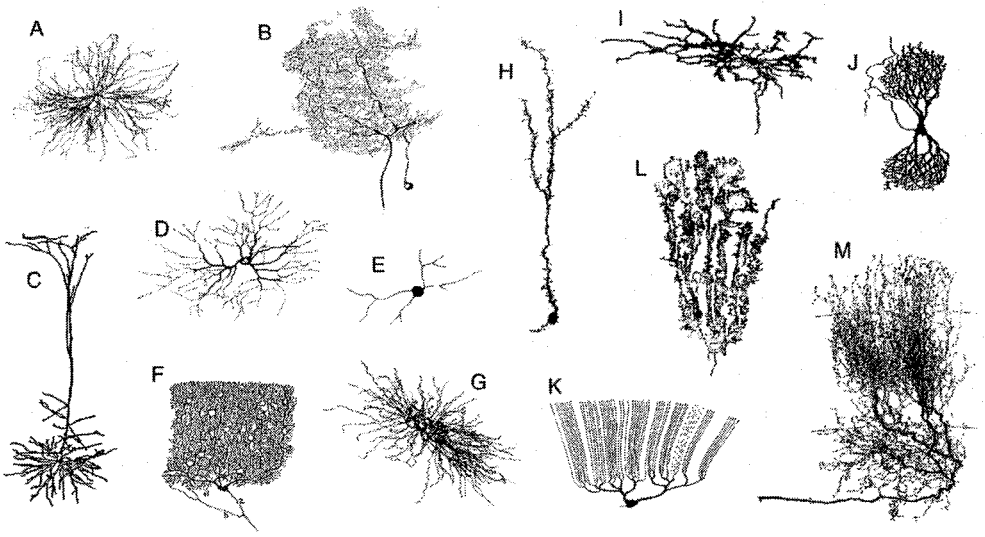

Fig. 3.1 DENDRITIC TREES OF THE WORLD Great variety of dendritic trees (in addition to a glia cell and an axonal tree) observed in the nervous systems of animals. The cells are not drawn to scale. **(A)** α motoneuron in spinal cord of cat (2.6 mm). Reprinted by permission from Cullheim, Fleshman, and Burke (1987). **(B)** Spiking interneuron in mesothoracic ganglion of locust (0.54 mm). Unpublished data from G. Laurent, with permission. **(C)** Layer 5 neocortical pyramidal cell in rat (1.03 mm). Reprinted by permission from Amitai et al., (1993). **(D)** Retinal ganglion cell in postnatal cat (0.39 mm). Reprinted by permission from Maslim, Webster, and Stone (1986). **(E)** Amacrine cell in retina of larval tiger salamander (0.16 mm). Reprinted by permission from Yang and Yazulla (1986). **(F)** Cerebellar Purkinje cell in human. Reprinted by permission from Ramón y Cajal (1909). **(G)** Relay neuron in rat ventrobasal thalamus (0.35 mm). Reprinted by permission from Harris (1986). **(H)** Granule cell from olfactory bulb of mouse (0.26 mm). Reprinted by permission from Greer (1987). **(I)** Spiny projection neuron in rat striatum (0.37 mm). Reprinted by permission from Penny, Wilson, and Kitai (1988). **(J)** Nerve cell in the nucleus of Burdach in human fetus. Reprinted by permission from Ramón y Cajal (1909). **(K)** Purkinje cell in mormyrid fish (0.42 mm). Reprinted by permission from Meek and Nieuwenhuys (1991). **(L)** Golgi epithelial (glia) cell in cerebellum of normal-reeler mouse chimera (0.15 mm). Reprinted by permission from Terashima et al., (1986). **(M)** Axonal arborization of isthmotectal neurons in turtle (0.46 mm). Reprinted by permission from Sereno and Ulinski (1987). The lengths given are approximate and correspond to the maximal extent. Reprinted by permission from Mel (1994).

defined Y cells correspond to the anatomically defined α ganglion cells while x corresponds to β (Saito, 1983; Stanford and Sherman, 1984). Figure 3.2 shows the dendritic tree and the cell body of an β cell, including its presynaptic input from bipolar cells, reconstructed from serial electron micrographs (Freed and Sterling, 1988). Because a cell can only respond to light stimulation in that part of the retina where it has functional connections with the photoreceptors (via horizontal and bipolar) cells, it is not surprising that the position, shape, and size of the receptive field are determined by the position, shape, and size of the underlying dendritic tree (Fig. 3.3). Indeed, a compartmental model of the type discussed in this chapter has shown that the passive electrotonic properties of the dendritic tree itself contribute very little to the spatial profile (Freed, Smith, and Sterling, 1992). Because of the horizontal spread of the neuronal elements interposed between the photoreceptors, the receptive field is on average 1.4 times larger than the dendritic tree.

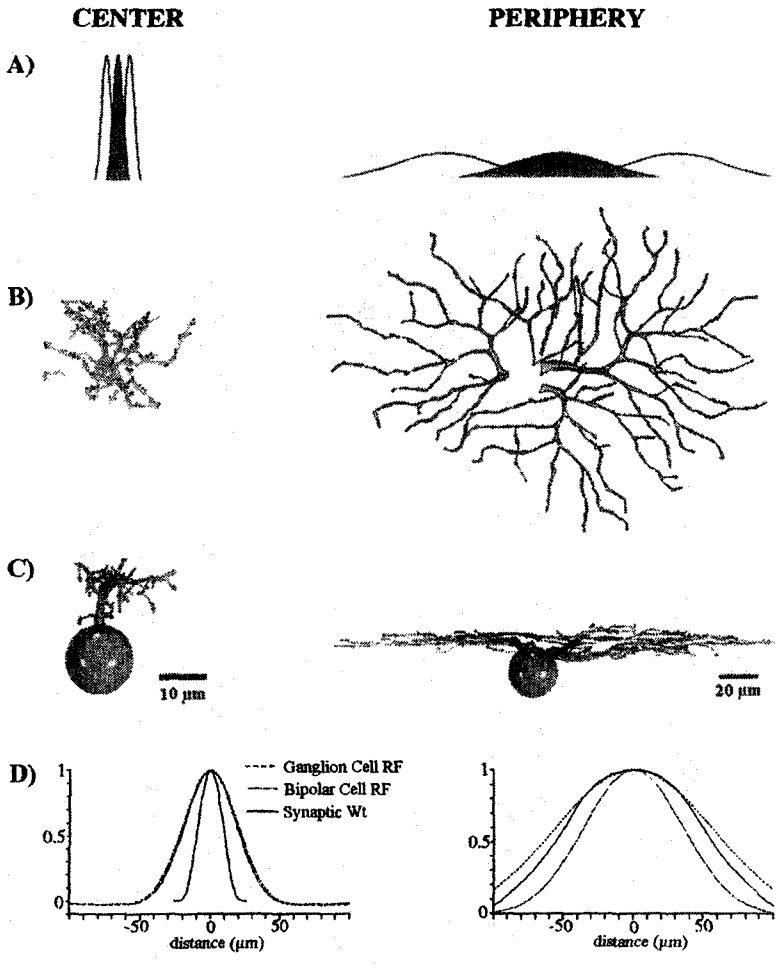

Fig. 3.2 STRUCTURE-FUNCTION RELATIONSHIP IN RETINAL GANGLION CELLS The relationship between the extent of the receptive field of visual neurons and the size of their dendritic tree differs depending on the size of the receptive field. Shown here is the functional architecture of a central (1°; left column) and a peripheral (20°; right column) β ganglion cell in the cat retina. **(A)** Receptive field of these cells, determined by fitting a Gaussian sensitivity curve through their center (dark) and their surround fields. **(B)** Their dendritic tree, reconstructed at the electron-microscopic (left) and the light-microscopic (right) levels. The small cell receives excitatory input from about 170 bipolar ribbon synapses, while the large one is excited by 1700 bipolar ribbon synapses (see Fig. 1.5). **(C)** Compartmental modeling of these two cells, assuming a passive dendritic tree, shows that voltage attenuation is negligible. **(D)** The receptive field of the two ganglion cells, obtained from the literature, is superimposed onto the receptive field of the presynaptic neuron, a bipolar cell. The effect of synaptic input from the bipolar cell onto the ganglion cell—expressed by the dendritic tree itself—is summarized by the "synaptic weight" curve. For a central β cell, it contributes little to the ganglion cell receptive field, since the input receptive field is substantially broader than the contribution from synaptic input onto the dendritic tree (solid inner curve in the left panel). Since the dendritic tree contribution for a cell in the periphery (solid middle curve in the right panel) is larger than the extent of the receptive field of the input, it gives rise to the observed linear scaling of the receptive field with the dendritic tree size for large cells. Unpublished data from P. Sterling and R. Smith, printed with permission.

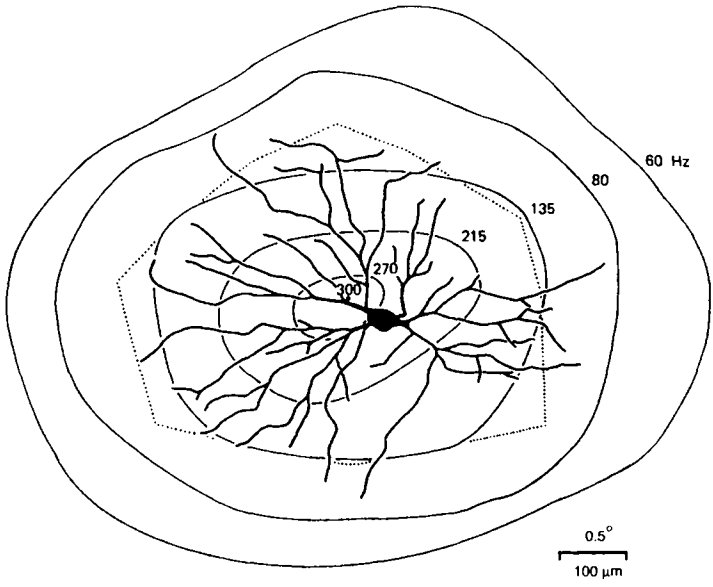

Fig. 3.3 RELATIONSHIP BETWEEN RECEPTIVE-FIELD SIZE AND DENDRITIC TREE Comparison of the dendritic tree and the receptive field center, shape, and extent of a retinal ganglion cell in the cat. Morphologically, this cell type is known as α; its axon (not shown) projects to the geniculate. The continuous contour lines correspond to equal response contours and represent peak firing rates of the indicated amount in response to a flashing spot of light. The maximum discharge of 300 spikes per second is marked by a spot. The maintained background activity of the cell was 32 Hz. The dotted line corresponds to the cell's receptive field. The physiologically defined receptive field extends roughly 100–150 μm beyond the dendritic tree. Reprinted by permission from Peichl and Wässle (1983).

A very similar structure-function relationship also holds for the anatomically defined β class of cat retinal ganglion cells in the periphery, where the dendritic tree of these cells is relatively large (Fig. 3.2). This cell type corresponds to the physiologically defined X type (Saito, 1983; Stanford and Sherman, 1984). The proportionality between receptive field size and the extent of the dendritic tree fails for small β type ganglion cells near the center of the retina. Here, the receptive field of the presynaptic neurons providing the driving input, bipolar cells, is already substantially larger in extent than the dendritic tree of the ganglion cell, obscuring any contribution the passive dendritic tree might make.

Besides this simple size relationship, what other functional aspects might the different retinal ganglion cell morphologies reflect? And what about possible structure-function relationships of other cell types? In the periphery, one can expect specific structural elements of the nervous system to reflect specific attributes of the physical world they are designed to extract. This is unlikely to be the case for more central structures. Can one still say *something meaningful* about how information processing is related to different dendritic trees (Borst and Egelhaaf, 1994)?

In this chapter, central to the book, we discuss how the previously introduced concepts from linear cable theory can be applied to study the electrical properties of complex, spatially extended dendritic trees. Why should the reader study passive dendritic trees when evidence from calcium imaging experiments, coupled with intradendritic recordings, shows that most, if not all, dendritic trees include substantial voltage-dependent, that is, nonlinear membrane

components? This challenge can be answered by citing the truism "You can't run before you can walk." An understanding of information processing in active trees can only be based upon knowing the properties of passives ones. Furthermore, under certain well-specified conditions, for instance, for "small" synaptic inputs, voltage-dependent nonlinearities do not come into play and the dendrite acts essentially like a passive one. Let us therefore press on, delaying the confrontation with active trees until Chap. 19.

3.1 Branched Cables

An extended dendritic tree can be treated as a branched cable structure, where each cable or cylinder can, in principle, have different diameters and membrane properties. Since there exists no evidence for loops within a given dendritic tree structure, that is, one dendritic branch connecting—either directly or with the aid of a synapse—to another dendrite of the same cell, dendritic arbors can be considered to be true *trees* in the graph theoretic sense, with a unique path between any two points in the tree.

3.1.1 What Happens at Branch Points?

The cable equation (Eq. 2.7) as applied to a finite cable holds for any particular unbranched cylindrical segment with constant membrane properties and a constant diameter. How can we use this equation to study the potential in two or more such segments connected together? The way in which finite cable segments are linked resides in the appropriate choice of boundary conditions for each segment. In order to understand this better, let us focus on the highly simplified dendritic tree illustrated in Fig. 3.4A. We assume that the three branches have electrotonic lengths L_0, L_1, and L_2, with infinite input resistances $R_{\infty,0}$, $R_{\infty,1}$, and $R_{\infty,2}$. As discussed in Sec. 2.2.2, the *infinite input resistance* of a finite cable is equal to the input resistance of a semi-infinite cable of the same diameter and having the same R_m and R_i values, looking toward the infinitely far away terminal, and is computed according to Eq. 2.16.

We will assume, for the sake of simplicity, that the two rightmost branches terminate with a sealed-end boundary condition. The input resistances of the two rightmost daughter branches at the branch point, looking toward their terminals, are specified by Eq. 2.21 as

$$R_{\text{in},1} = R_{\infty,1} \coth(L_1) \tag{3.1}$$

and

$$R_{\text{in},2} = R_{\infty,2} \coth(L_2) . \tag{3.2}$$

For an arbitrary boundary condition at the rightmost terminal of the daughter branches (rather than the sealed end assumed here) we replace these expressions by Eq. 2.28.

The right-hand side of the main cable ends at the branch point with the two daughter cables. Its terminal resistance $R_{L,0}$ is determined by the input resistances of the daughter branches, by making use of the fact that the net conductance of two parallel conductances is simply given by their sum. In other words, we compute the terminal resistance by effectively replacing the two conductances of the daughter branches by a single one. The effective terminal resistance of the main cable is given by

$$\frac{1}{R_{L,0}} = \frac{1}{R_{\text{in},1}} + \frac{1}{R_{\text{in},2}} . \tag{3.3}$$

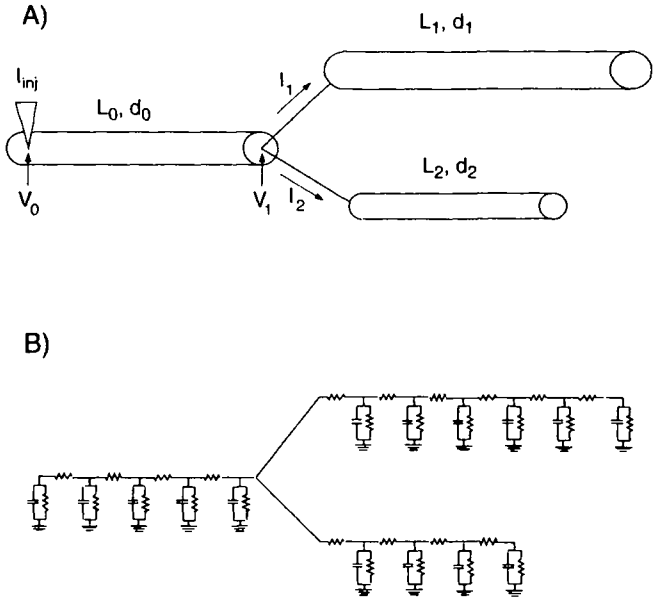

Fig. 3.4 PASSIVE BRANCHING DENDRITE **(A)** Schematic drawing of a passive cylindrical dendrite, with diameter d_0 and electrotonic length $L_0 = l_0/\lambda_0$, with two daughter branches, each with its distinct diameter and electrotonic length $L_i = l_i/\lambda_i$. A simple recursive scheme exists to compute exactly the voltage in such tree structures in response to current input (Rall, 1959). All terminals are assumed to be sealed. **(B)** Compartmental-model representation of this passive dendritic tree. The voltage dynamics in this circuit approximate the solution to the cable equation of the continuous cable in **A** in the sense that the cable equation (Eq. 2.7) describes the dynamics of the membrane potential in the limit that the grid size becomes infinitely fine. For the sake of simplicity, we set V_{rest} to zero (see Fig. 2.3). Standard software packages, such as NEURON or GENESIS, automatically solve for the voltage in these circuits.

In a final step, we apply Eq. 2.28 to arrive at the input resistance at the left terminal of the main branch (looking toward the daughter branches),

$$R_{in,0} = R_{\infty,0} \frac{R_{L,0} + R_{\infty,0} \tanh(L_0)}{R_{\infty,0} + R_{L,0} \tanh(L_0)}. \tag{3.4}$$

The same algorithm can, of course, be applied in a recursive manner to evaluate the input resistance of arbitrary passive trees. Moving from the outermost dendritic tips and using either Eq. 2.21 or Eq. 2.24 (depending on the choice of boundary conditions), we compute the input resistances of the daughter branches. Adding the inverse of these input resistances gives the inverse of the terminal resistance of the branch of the parent generation. We now use Eq. 2.28 to compute the input resistance of this branch and its sibling, add them in parallel, and so on. Of course, this "folding" algorithm needs to be carried out on both ends of the cylinder. (In our pedagogical example in Fig. 3.4, we did not consider the effect of one or more cables connecting to the left terminal of the parent cable.) In this manner, the input resistance at any point in the tree can be evaluated exactly, a procedure proposed by Rall (1959) and described in considerable detail in Chap. 7 of Jack, Noble, and Tsien (1975).

Once we compute the input resistance at any particular location in the dendritic tree, we can derive the steady-state voltage at that location in response to a current injection I_{inj} using Ohm's law. For instance, the voltage at $x = 0$ in the parent cable is

$$V_0 = R_{\text{in},0} \cdot I_{\text{inj}} . \tag{3.5}$$

Given V_0, we can use Eq. 2.27 to compute the sustained voltage change anywhere along the main branch in response to the sustained current injection I_{inj}. Furthermore, recursive evaluation of this equation allows us to compute the voltage at any location in the tree of Fig. 3.4. Altogether, four linear equations (Eqs. 2.27, 2.28, 3.3, and 3.5) need to be applied iteratively to solve for the input resistance, and therefore for the sustained voltage following a sustained current input, in any dendritic tree structure in response to a current injection at any location (Rall, 1959).

Assuming that the parent cable delivers the current I_0 to the two daughter branches, what fraction I_1 of this current will flow into one and what fraction I_2 into the other (Fig. 3.4A)? Using Eqs. 2.2 and 2.20 and the definition in Eq. 2.16, we compute the current flowing in one of the daughter cables, assuming that its terminal is sealed (this is not necessary),

$$I_1(X) = \frac{V_1}{R_{\infty,1}} \frac{\sinh(L_1 - X)}{\cosh(L_1)} \tag{3.6}$$

where V_1 is the voltage at the branch point. At this point, $X = 0$ (for the daughter branch), and the current flowing into this branch is given by

$$I_1(X = 0) = \frac{V_1}{R_{\text{in},1}} \tag{3.7}$$

where we made use of Eq. 3.1. Since the same principle applies to the second daughter branch and also holds true for an arbitrary boundary condition (in this case Eq. 2.20 must be replaced by Eq. 2.27), it follows that

$$I_0 = I_1 + I_2 = V_0(G_{\text{in},1} + G_{\text{in},2}) \tag{3.8}$$

where $G_{\text{in},1} = 1/R_{\text{in},1}$ and likewise for $G_{\text{in},2}$. In other words, the current divides among these branches according to their input conductances.

3.2 Equivalent Cylinder

Under certain conditions one does not need to solve numerous equations to derive the potential in a branched tree, a great simplification discovered and exploited by Rall (1962, 1964). Let us compute the voltage distribution in the simple tree shown in Fig. 3.4, assuming that the two daughter branches are identical (that is, $L_1 = L_2$ and $d_1 = d_2$ with identical membrane parameters) and that a sustained current is injected into the left terminal of the parent cylinder. The normalized voltage profile throughout this minitree is illustrated in Fig. 3.5 for three different combinations of parent and daughter branch diameters: (1) $d_0 = 2d_1$, (2) $d_0^{3/2} = 2 \cdot d_1^{3/2}$, and (3) $d_0 = d_1$. The upper and lower curves indicate the two limiting cases in which the parent cable is terminated at the right end either with a sealed-end boundary condition or in a short circuit. In the cases where the parent diameter has either twice the diameter or the same size as the daughter branches, close inspection of the curves in Fig. 3.5 reveals a discontinuity in the derivative of the voltage at the branch point.

In the third case, $d_0^{3/2} = 2d_1^{3/2}$, all derivatives of the voltage profile are continuous and a rather interesting phenomenon occurs. In contrast to the other two cases, the voltage decay along both sets of cables can be described by a single expression. To see why, let us return

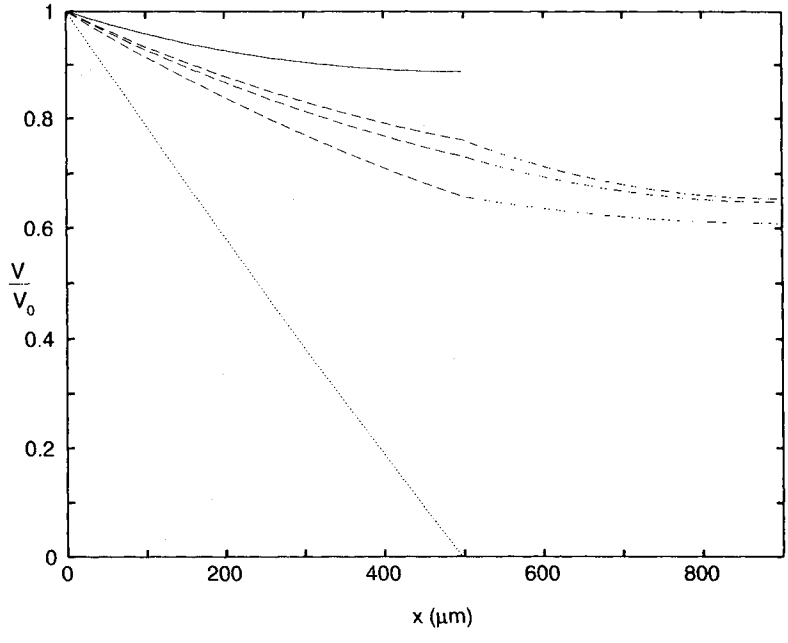

Fig. 3.5 VOLTAGE DECAY ALONG A SIMPLE DENDRITIC TREE Steady-state voltage decay along the tree shown in Fig. 3.4A, assuming that the two daughter branches are identical, with $d_1 = d_2$ and $L_1 = L_2 = 0.5$. The three dashed curves correspond to (1) $d_0 = 2d_1$, (2) $d_0^{3/2} = 2d_1^{3/2}$, and (3) $d_0 = d_1$. For the dotted curve, the potential at the right-hand terminal of the main branch is set to zero (short circuit). For the upper, continuous curve, the membrane is sealed. At the branchpoint $x = 500\,\mu$m, the voltage profile has a discontinuous derivative for $d_0 = 2d_1$ and for $d_0 = d_1$. If the input resistance of the parent at this point is matched to that of the daughter branches (as is the case for the second condition, $d_0^{3/2} = 2d_1^{3/2}$), the voltage decay across the cables can be described by a single, simple expression. This trick is exploited by Rall in his concept of the *equivalent tree*.

to Eq. 2.27, expressing the voltage in a finite cable of length L_0 with an arbitrary terminal condition specified via the terminal resistance $R_{L,0}$,

$$V(X) = V_0 \cdot \frac{R_{L,0}\cosh(L_0 - X) + R_{\infty,0}\sinh(L_0 - X)}{R_{L,0}\cosh(L_0) + R_{\infty,0}\sinh(L_0)} . \tag{3.9}$$

Since both daughter cables are identical and therefore have identical input resistance, $R_{\text{in},1} = R_{\text{in},2}$ (Eqs. 3.1 and 3.2), it follows from Eq. 3.3 that the combined input resistance of both cables is

$$R_{L,0} = \frac{R_{\infty,1}\coth(L_1)}{2} . \tag{3.10}$$

We now return to Eq. 2.16 for the input resistance of a semi-infinite cable, noticing its dependency on the inverse of the cable diameter to the $\frac{3}{2}$ power

$$R_{\infty,0} = \left(\frac{R_m \cdot R_i}{\pi^2}\right)^{1/2} \frac{2}{d_0^{3/2}} . \tag{3.11}$$

If $d_0^{3/2} = 2d_1^{3/2}$, then

$$R_{\infty,0} = \frac{R_{\infty,1}}{2} . \tag{3.12}$$

That is, the infinite input resistance of the parent cable is matched to the infinite input resistances of the two daughter branches in parallel. Combining Eqs. 3.10 and 3.12 leads to

$$R_{L,0} = R_{\infty,0} \coth(L_1) . \tag{3.13}$$

If we place this back into Eq. 3.9, we have

$$\begin{aligned} V(X) &= V_0 \cdot \frac{\cosh(L_0 - X) + \sinh(L_0 - X)/\coth(L_1)}{\cosh(L_0) + \sinh(L_0)/\coth(L_1)} \\ &= V_0 \frac{\cosh(L_0 + L_1 - X)}{\cosh(L_0 + L_1)} . \end{aligned} \tag{3.14}$$

Comparing this to Eq. 2.20, we see that the above equation describes the voltage in a single, unbranched cylinder of length $L_0 + L_1$ with a sealed-end boundary condition. Instead of having to model this structure as three interconnected cylinders, we can reduce it to a single *equivalent cylinder*, whose electrotonic length is given by $L_0 + L_1$ and whose diameter is identical to the diameter of the main branch. The reason we are able to carry out this simplification is that the infinite input resistance of the main branch is "matched" to the infinite input resistance of the two daughter branches in parallel, a principle known as *impedance matching*. In particular, the voltage and the input resistance now have continuous derivatives across the branch point, as witnessed in Fig. 3.5. Note that, in general, impedance matching does not imply that the input resistance R_{in} of the daughter cables is matched to that of the main cable (since the input resistance of the main cable at the right terminal is proportional to $\coth(L_0)$ while the input resistance of the daughter branches is proportional to $\coth(L_1)$).

As Rall (1962, 1964) first showed in the early 1960s, an entire class of dendritic trees can be reduced or collapsed into a single equivalent cylinder provided the following four conditions are met. (1) The values of R_m and R_i are the same in all branches. (2) All terminals end in the same boundary condition. (3) All terminal branches end at the same electrotonic distance L from the origin in the main branch, where L is the sum of the L_i values from the origin to the distal end of every terminal; L corresponds to the total electrotonic length of the equivalent cylinder. (Note that this requirement does not necessarily include only trees with perfect symmetric branching.) (4) At every branch point, infinite input resistances must be matched. If all cables possess the same membrane resistance and intracellular resistivity, this implies

$$d_0^{3/2} = d_1^{3/2} + d_2^{3/2} . \tag{3.15}$$

This last condition is known as the $d^{3/2}$ law. If these four conditions are met, the equivalent cylinder mimics perfectly the behavior of the entire tree. In other words, injecting current into the leftmost terminal of the tree will yield exactly the same voltage response as injecting the identical current into its equivalent cylinder.

If input to any of the daughter branches is considered, an additional constraint must be obeyed. (5) Identical synaptic inputs, whether current injection or conductance change, must be delivered to all corresponding dendritic locations. In the case of Figs. 3.4 and 3.5, injecting a current I_0 into both daughter branches at the same electrotonic distance X_1 from the branch point corresponds to injecting the current $2I_0$ into the equivalent cable at location $X = L_0 + X_1$. If we are only interested in describing the voltage in the primary branch, because this is close to the cell body where the intracellular electrode is usually located, injecting the current $2I_0$ into only one of the two daughter branches will lead to the same

voltage change in the primary branch as injecting the current $2I_0$ at the distance $L_0 + X_1$ in the equivalent tree (Rall and Rinzel, 1973). This ceases to be true when considering the voltage profile in other parts of the equivalent tree, outside of the region $X \leq L_0$.

The transformation from a branching cable structure to an equivalent cylinder preserves membrane area. In other words, the branching tree has the same membrane surface area as the unbranched cylinder that has the same diameter as the trunk of the tree and the same electrotonic length as the whole dendritic tree. This implies that all variables that are expressed per unit membrane area, such as channel densities, R_m, and C_m, are conserved in the transformation to an equivalent cylinder.

The principle of impedance matching is a powerful one and can be generalized to many situations. While here we have only considered the case of stationary inputs, the reduction of a tree to a cylinder can also be carried out for transient inputs, as long as the above four conditions are satisfied and C_m is constant throughout the entire tree. In other words, the dynamic behavior of the voltage is identical in the two cases. Furthermore, impedance matching can be generalized to tapering cables (Rall, 1962) and even holds in the presence of an active membrane containing voltage-dependent elements. In particular, axonal trees fulfilling the above conditions can similarly be reduced to a single equivalent axon.

Rall exploited this technique to great advantage in his extensive research on the electrical behavior of cat α motoneurons (Rall, 1977; Rall et al., 1992; see also Fleshman, Segev, and Burke, 1988), where the somatic potential of the cell in response to synaptic input in the dendritic tree is modeled by a single equivalent cylinder with the cell body being represented by an RC element tacked onto one end of the cylinder. Under these conditions, the electrical behavior of an entire neuron is characterized by a simple model with six free parameters (the R and C values of the isopotential soma, the R_m, C_m, and R_i of the equivalent cylinder, as well as its electrotonic length L).

Real dendritic trees rarely conform to all of the assumptions underlying the equivalent tree reduction. In some cases the $d^{3/2}$ rule is observed to a remarkable extent at branch points (e.g., relay cells in the cat's lateral geniculate; Bloomfield, Hamos, and Sherman, 1987). In general, neither this local rule dictating the diameter of branching processes nor the assumption that all dendrites terminate at the same distance from the cell body hold (Hillman, 1979; Burke, 1998; Larkman et al., 1992; Turner et al., 1995).

With a few exceptions, then, most neurons violate one or more of the constraints required for reducing a tree to an equivalent tree. In fact, one can ask why should dendritic trees obey the $d^{3/2}$ law at all? What functional advantages can be realized for a neuron if its dendritic tree can be reduced to a single equivalent cylinder? Voltage "reflections" at branch points will be absent if the $d^{3/2}$ law is obeyed, but it is unclear why this should be relevant to neurons.[2]

3.3 Solving the Linear Cable Equation for Branched Structures

Historically, much effort was spent on deriving solutions to linear differential equations like the cable equation in terms of series expansions of specialized functions (such as Bessel functions) and we will briefly touch upon these methods. Yet, given the widespread usage of digital computers and the complicated geometries of cells as well as their non-linear membrane characteristics, the majority of research today is being carried out using numerical methods.

2. Concepts from the *matched transmission lines* literature in electrical engineering are germane to some of these questions. We will not pursue any of the interesting analogies; see Davidson (1978) or Brühl, Jansen, and Vogt (1979).

3.3.1 Exact Methods

A number of iterative techniques have been developed to solve exactly for the voltage transient in treelike structures in response to an arbitrary current input $I(t)$. All of them rely on the superposition principle, that is, on the linearity of the membrane (although a linear membrane need not necessarily be passive; see Chap. 10).

Linearity of the membrane implies that the injection of a sinusoidal current of frequency f only gives rise to a voltage response at the same frequency. The above equations can be reformulated in the Laplace (or Fourier) domain to compute the potential $\tilde{V}(f)$ anywhere in the tree in response to a sinusoidal current $I(t) = I_0 \sin(2\pi f t)$ applied anywhere else. One set of methods (Butz and Cowan, 1974; Horwitz, 1981; Koch, 1982; Koch and Poggio, 1985a; Holmes, 1986) uses variants of this approach to derive $\tilde{V}_m(f)$ in arbitrary dendritic trees with the help of a small number of rules. Usually, these equations have simple graphical interpretations and can be implemented recursively, leading to very efficient and small programs.

For instance, Koch and Poggio's (1985a) four rules specify the impedance of a single cylinder (Eq. 2.28), the effective impedance at a branch point (Eq. 3.3), and the voltage at any point in a cylinder as a function of either the injected current (by combining Eqs. 2.25 and 2.26) or the voltage at one terminal (Eq. 2.27). One advantage of this method is that it can be applied to evaluate the potential in dendritic trees with arbitrary linear membranes, such as those containing inductances as can be obtained by linearizing certain active types of membranes (see Chap. 10). The number of equations that need to be evaluated in these methods is proportional to the number of cylindrical segments in the dendritic tree considered. Note that these methods require the inverse Laplace (or Fourier) transform to obtain $V(t)$.

A completely different approach was pioneered by Abbott and his group (Abbott, Farhi, and Gutmann, 1991; Abbott, 1992; Cao and Abbott, 1993), based on a path integral approach of the type used so successfully in quantum mechanics and quantum field theory (Feynman and Hibbs, 1965). The voltage at x in response to current input at y in an arbitrary tree (including trees with loops) is obtained by evaluating the Green's function of the cable (for example, Eq. 2.31) along all possible "paths" between x and y. The number of paths is potentially infinite, since a path, starting out at point x and heading toward y, may change direction at every node or terminal it encounters on its way and may pass through x and y an arbitrary number of times but must begin at x and end at y. Of course, the longer the path, the smaller its final contribution toward the potential. (The Green's function in Eq. 2.31 suppresses long paths of length L_{path} exponentially as $e^{-L^2_{\text{path}}/4T}$.) We met such an approach while evaluating the potential in a single finite cylinder by summating over infinitely many reflecting terms (Eq. 2.41 and Fig. 2.10). The primary advantage of this method lies in computing $V(t)$ explicitly for short times, since under these conditions only as few as four paths need to be evaluated (Cao and Abbott, 1993). Furthermore, distinct from the methods working in the Laplace/Fourier domain, the path integral method yields the membrane potential directly as a function of time.

3.3.2 Compartmental Modeling

All the algorithms discussed so far solve for $\tilde{V}_m(f)$ and $V_m(t)$ in response to an arbitrary current input $\tilde{I}(f)$ and $I(t)$, respectively. They come, though, with serious drawbacks. (1) In the presence of n current inputs—rather than a single one—on the order of n^2 additional computations have to be performed (see Sec. 3.3); that is, these methods do not at all scale

well to massive synaptic input. (2) While these methods can be adapted to treat synaptic input as conductance changes, it is not computationally efficient to do so. (3) Finally, and fatally, they assume linearity and fail in the presence of voltage-dependent membrane components.

The method of choice for most work in the field is to solve the partial differential equations numerically by discretizing the underlying equations. This approach, introduced by Rall in his landmark (1964) paper (see also Segev, Rinzel, and Shepherd, 1995), is known as *compartmental modeling* and leads to the discrete electrical circuits illustrated in Fig. 3.4B. Instead of solving the continuous, linear or nonlinear, partial differential cable equation, it is discretized into a system of ordinary differential equations, corresponding to small patches of neuronal membrane that are isopotential. These compartments are then coupled by sparse matrices.

The most fundamental requirement of any numerical method is *convergence*, that is, that the error between the solution using the numerical method and the exact solution be made as small as possible. Furthermore, the method must be stable. These requirements place constraints on how fine time and space must be discretized in order to arrive at an—approximately—correct solution. A conservative rule of thumb is to divide the cable into segments equal to or smaller than one-tenth of the associated effective length constant λ (Segev et al., 1985). How to achieve all of this properly and in an as efficient manner as possible is a well-established subject within applied mathematics. Appendix C, written by Barak Pearlmutter and Anthony Zador, treats modern numerical techniques—using the matrix formalism—for approximating the solution of these equations.

A number of public-domain single-cell simulators with graphical interfaces, in particular NEURON and GENESIS, implement such methods in an efficient manner. (For an overview of about half a dozen of them see DeSchutter, 1992; for more comprehensive references see Bower and Beeman, 1998 and Koch and Segev, 1998.) Indeed, the field has advanced to such a point that a set of benchmarks has been introduced to compare simulators in a more quantitative manner (Bhalla, Bilitch, and Bower, 1992).

The power of compartmental methods derives from their flexibility in permitting arbitrary levels of functional resolution to be included into the model. As long as the mechanism at hand, say a particular membrane conductance or pump, can be described by a steady-state or a differential equation, it can be incorporated into the model. Indeed, the numerical simulations discussed in this book range from the submillisecond to the second scale and from the submicrometer regime to several millimeters. Ultimately, the limiting factor in erecting ever more complex models is the exploding number of functions and parameters that need to be specified and measured as well as the speed of the computer implementing the algorithm.

3.4 Transfer Resistances

Let us now introduce a different, and much more intuitive, manner of calculating the voltage change in response to current input in passive dendritic trees of arbitrary geometry. Rather than expressing the properties of some electrical network in terms of an analytical expression figuring the various cellular parameters (e.g., the Green's function Eq. 2.31), the system is "observed" at one, two, or more discrete locations, and its properties are summarized in terms of a handful of functions called *transfer functions*. Their usage is based on multiport theory, in which a linear or nonlinear system is characterized by n ports, or independent pairs of current and voltage at each port (Oster, Perelson, and Katchalsky, 1971; Chua, Desoer and Kuh, 1987; Wyatt, 1992). Resistance, diode, capacitance, or inductance are all

instances of one-port devices, since a pair of numbers, the voltage across the device and the current through it, completely captures their behavior, while the simplest model of a bipolar transistor is a three-terminal element (collector, emittor and base) with two pairs of current-voltage relationships. As we will see in Chap. 4, a chemical synapse can also be approximated as a two-port device (at a short time scale).

The two-port formulation of cable theory, in which voltage and current are manipulated at two locations in an arbitrary tree, has proven to be of great intuitive value. In particular, it allows the attenuation experienced by synaptic input on its way to the soma to be easily expressed. In the version popularized by Butz and Cowan (1974) (see also Fig. 3.6 and Koch, Poggio, and Torre, 1982; Carnevale and Johnston, 1982) it assumes that the dendritic tree is linear (although n-port theory does not require this straight-jacket).

3.4.1 General Definition

As long as one is dealing with a linear system, the voltage change $V_j(t)$ at location j in response to an arbitrary current input $I_i(t)$ at location i can always be expressed as

$$V_j(t) = K_{ij}(t) * I_i(t)$$
$$= \int_{-\infty}^{+\infty} K_{ij}(t')I_i(t-t')dt' = \int_0^t K_{ij}(t')I_i(t-t')dt' , \qquad (3.16)$$

where $K_{ij}(t)$ is the *impulse response* or *Green's function* of the system (Fig. 3.6). The last relationship assumes that the impulse function is *causal*, implying that $K_{ij}(t) = 0$ for $t \leq 0$ (since no effect can precede its cause) and that no current is injected prior to $t = 0$.

The subscripts ij signify that the current is injected at i and the voltage recorded at j, a convenient mnemonic short form for summarizing the input-output relationship. Equation 3.16 holds for any cable structure and simply expresses the linearity of the system. The Green's function can be obtained by injecting a delta pulse of current into the cable, that is, $I_i(t) = I_0\delta(t)$, and computing $V_j(t)$ by solving the appropriate cable equation. This yields

$$K_{ij}(t) = \frac{V_j(t)}{I_0} \qquad (3.17)$$

with the dimension of a resistance. If location i coincides with location j, the equation reduces to

$$V_i(t) = K_{ii}(t) * I_i(t) . \qquad (3.18)$$

One way to visualize the meaning of $K_{ij}(t)$ is to compute its Fourier transform (see Appendix B) $\tilde{K}_{ij}(f)$, where f is the temporal frequency in units of hertz. It is a complex

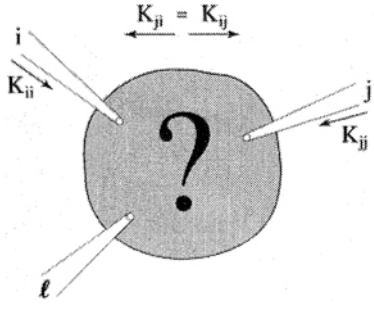

Fig. 3.6 Transfer Functions Neuronal transfer functions are used throughout the book to characterize an arbitrarily complex, but linear neuron. The unknown system is observed at two points, or ports, i and j. The behavior at these two points can be fully described by knowledge of the three transfer functions K_{ii}, $K_{ij} = K_{ji}$, and K_{jj}. In particular, the attenuation of the input at i propagating to j can be easily expressed in terms of these functions. Its chief drawback is that these functions are not useful for expressing the voltage at some other location ℓ. This requires knowledge of $K_{i\ell}$ and $K_{\ell\ell}$.

function whose amplitude is measured in ohms. Any particular value of $\tilde{K}_{ij}(f)$ can be measured by injecting a sinusoidal current of frequency f at location i, that is, $I_i = \sin(2\pi f t)$, and recording the resultant voltage amplitude and phase at location j at the same frequency f.

The steady-state voltage change in response to a stationary current (that is, for $f = 0$) can be recovered with the aid of the real number

$$\tilde{K}_{ij}(f = 0) = \int_0^{+\infty} K_{ij}(t)dt\,. \tag{3.19}$$

We follow the practice of referring to the complex function $\tilde{K}_{ij}(f)$ as the *transfer impedance*, to its stationary or dc value $\tilde{K}_{ij}(f = 0) > 0$ as the *transfer resistance*, and to its inverse as the *transfer conductance*. Unless otherwise noted, $\tilde{K}_{ij}$ refers to $\tilde{K}_{ij}(f = 0) > 0$. Similarly, the amplitude of $\tilde{K}_{ii}(f)$ is called the *input impedance* and $\tilde{K}_{ii}(f = 0) > 0$ the *input resistance*.

3.4.2 An Example

In order to relate transfer resistances to the previously computed Green's functions, let us consider events in an infinite, passive cable of diameter d. Following Eq. 2.31 we can directly write

$$K_{ij}(T) = \frac{R_m}{2\pi d\lambda(\pi T)^{1/2}}\, e^{\frac{-(|i-j|/\lambda)^2}{4T}}\, e^{-T} \tag{3.20}$$

where $|i - j|$ is a shorthand notation to represents the distance between i and j, that is, between the sites where the current is injected and the voltage is recorded, and $T = t/\tau_m$ is the normalized time. To compute K_{ii}, we set $|i - j|$ to zero,

$$K_{ii}(T) = \frac{R_m}{2\pi d\lambda(\pi T)^{1/2}}\, e^{-T}\,. \tag{3.21}$$

The Fourier transform of $K_{ij}(T)$ yields

$$\tilde{K}_{ij}(f) = \frac{R_\infty}{2}\frac{1}{\sqrt{1 + i2\pi f\tau_m}} e^{-\sqrt{1+i2\pi f\tau_m}|i-j|/\lambda} \tag{3.22}$$

where R_∞ is the input resistance of a semi-infinite cylinder (Eq. 2.16). For the transfer resistance at $f = 0$ we arrive at

$$\tilde{K}_{ij} = \frac{R_\infty}{2} e^{-|i-j|/\lambda} \tag{3.23}$$

and for the input resistance,

$$\tilde{K}_{ii} = \frac{R_\infty}{2}\,. \tag{3.24}$$

The transfer resistance decays exponentially with the distance between the two sites and indicates the degree of coupling between the two sites i and j, which decreases with increasing distance.

3.4.3 Properties of $\tilde{K}_{ij}$

We will now assume that we are dealing with current inputs that either are stationary or change much more slowly than the membrane time constant τ_m. Since this corresponds to

the solution of Eq. 3.16 with $t \to \infty$, the convolution is replaced by multiplication and the function $K_{ij}(t)$ is replaced by the dc component of its Fourier transform; that is,

$$V_j = \tilde{K}_{ij}(0) I_i = \tilde{K}_{ij} I_i \tag{3.25}$$

for the transfer resistance between i and j and

$$V_i = \tilde{K}_{ii}(0) I_i = \tilde{K}_{ii} I_i \tag{3.26}$$

for the input resistance at location i. Transfer and input resistances have several noteworthy properties.

Symmetry

The most important property is *symmetry*,

$$\tilde{K}_{ij} = \tilde{K}_{ji} . \tag{3.27}$$

If the current I_0 is injected at location i somewhere in the dendritic tree, and the voltage $V_0 = \tilde{K}_{ij} \cdot I_0$ is measured at location j, for instance, at the cell body, we obtain the same change in voltage V_0 at location i if the identical current I_0 is injected at location j: $V_i = \tilde{K}_{ji} \cdot I_j = \tilde{K}_{ij} \cdot I_0 = V_0$. This is true for any reciprocal linear system, irrespective of the positions of i and j. It is important to point out that this does not mean that the attenuation from location i to location j is the same as the other way around. Most emphatically not (see Sec. 3.5.2)!

Symmetry, in the electrical engineering literature also known as *reciprocity*, is a general property of n-ports created by interconnecting linear, two-terminal resistances. Its proof requires the use of Tellegen's theorem (Penfield, Spence, and Duinker, 1970; Reza, 1971) and is beyond the scope of this book.

Positivity

A second property is

$$\tilde{K}_{ij} \leq \tilde{K}_{ii} \quad \text{and} \quad \tilde{K}_{ij} \leq \tilde{K}_{jj} \tag{3.28}$$

from which it follows that the input resistance $\tilde{K}_{ii}$ is always larger than the transfer resistance between location i and any other location. Furthermore, the more removed i and j are, the smaller the transfer resistance $\tilde{K}_{ij}$. Thus, $\tilde{K}_{ij}$ is related to the degree of coupling of site i to site j.

Transitivity

A third property of any dendritic tree structure without loops is

$$\tilde{K}_{ij} = \frac{\tilde{K}_{i\ell} \tilde{K}_{\ell j}}{\tilde{K}_{\ell\ell}} \tag{3.29}$$

where ℓ corresponds to any location on the direct path between locations i and j. This relationship does not hold if ℓ is located on a branch off the direct path between i and j (Koch, 1982). For instance, if we consider the transfer resistance $\tilde{K}_{a3,s}$ between $a3$ and the soma in Fig. 3.7, Eq. 3.29 holds for points $a2$ and $a1$ but not for $a4$, $a11$, or $b1$. It can be viewed as a form of transitivity (as long as all three points are located along a direct path).

All three properties remain in force not only for the dc value of the transfer impedance but for any one frequency (e.g., $\tilde{K}_{ij}(f) = \tilde{K}_{ji}(f)$).

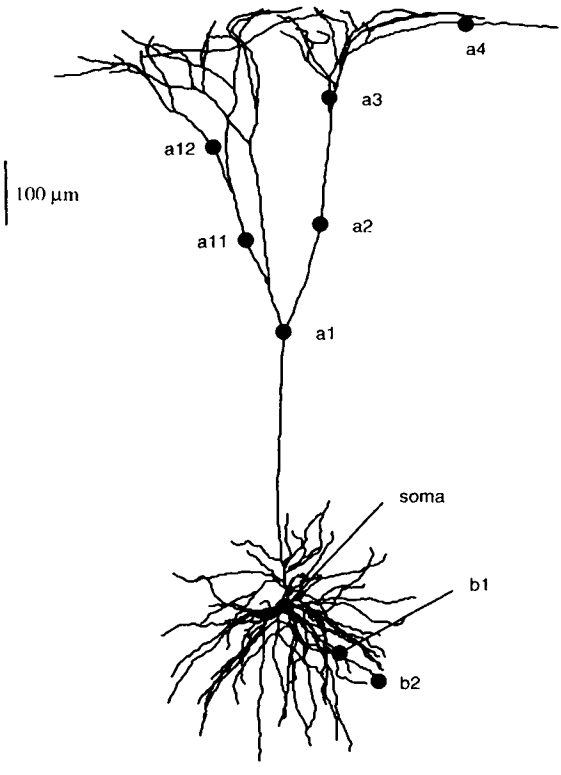

Fig. 3.7 A LAYER 5 NEOCORTICAL PYRAMIDAL CELL Morphology of the neocortical pyramidal cell we use throughout this book. The cell was stained and reconstructed by Douglas, Martin, and Whitteridge (1991) from the visual cortex of an adult cat. The cell body is located in layer 5 while the most distal dendrites lie in layer 1. A few locations that are used as synaptic input sites are indicated by letters.

While these properties are true for any cable system with a linear membrane, an additional property of cables with passive membranes is that the membrane becomes increasingly more conductive to current flow as the temporal frequency increases due to the presence of the capacitive element. Or,

$$|\tilde{K}_{ij}(f)| < |\tilde{K}_{ij}(f')| \tag{3.30}$$

for any $|f| > |f'|$. In particular, $\tilde{K}_{ij}(0) > |\tilde{K}_{ij}(f)|$. In other words, the transfer and input impedances show low-pass behavior. If the membrane contains inductive-like elements, caused, for instance, by the small signal behavior of a voltage-dependent potassium conductance activated by depolarization, $|\tilde{K}_{ij}(f)|$ can have a maximum at some nonzero frequency, with interesting consequences for information processing (see Chap. 10).

3.4.4 Transfer Resistances in a Pyramidal Cell

In order for the reader to develop his or her intuition about these transfer resistances and other related concepts in the following section, we will make use of our "canonical" model of a nerve cell, a pyramidal cell from the mammalian neocortex. We choose this particular neuron both for idiosyncratic reasons as well as for the general interest many scientists have in understanding the information processing operations occurring in cortex. Most of the concepts discussed in this book apply equally to other cell types.

The morphology of this neuron (Fig. 3.7) is derived from a layer 5 pyramidal cell in primary visual cortex filled with the intracellular dye HRP during experiments in the anesthetized adult cat (Douglas, Martin, and Whitteridge, 1991) and is translated into several

hundreds of compartments, similar to the ones shown in Fig. 3.4. The dendrites are passive while eight voltage-dependent membrane conductances at the cell body enable the cell to generate action potentials and shape the interspike interval between them accordingly (for details consult Bernander, 1993; Bernander et al., 1991, 1992, 1994). In this chapter we consider a linear model of the cell, obtained by replacing the active somatic membrane conductances by an appropriately chosen passive conductance, such that the input resistance and the resting potential throughout the cell are identical to the ones obtained in the full model. In other words, for small steady-state inputs this "passified" model behaves as the full, active model.

Unless otherwise noted, the ever-present spontaneous synaptic background activity has been incorporated into the passive membrane parameters. Because each transient opening of a synapse briefly increases the local membrane conductance, the random background activity will affect the "passive" membrane resistance R_m, with the effective membrane resistance varying from around 12,000 $\Omega \cdot cm^2$ at the soma to 52,000 $\Omega \cdot cm^2$ for distal dendrites (see Sec. 18.3). The membrane capacitance is set to 1 $\mu F/cm^2$ and the intracellular resistivity to 200 Ω·cm.

A number of the analytical techniques presented in Sec. 3.3 can be used to compute $\tilde{K}_{ij}$ in trees of arbitrary geometry, in particular the recursive techniques of Rall (1959), Butz and Cowan (1974), and Koch and Poggio (1985a). We refer the reader to these and other papers discussed in Sec. 3.3 and to Appendix C for more details. Table 3.1 shows representative values for $\tilde{K}_{ii}$ and $\tilde{K}_{is}$ for sustained and ac inputs. The steady-state input resistance $\tilde{K}_{ii}$ increases dramatically as one moves along the apical tree toward more distal sites, from 16.5 MΩ at the soma to several gigaohms in the far periphery. This is not unexpected, as we can see from Eq. 2.21 that the input resistance of a finite cable of electrotonic length L with a sealed end increases as $1/L$ as $L \to 0$, somewhat analogous to moving toward the distal dendritic tips. Using rapidly varying sinusoidal input of 10 or 1000 Hz reduces the input resistance moderately.

The transfer resistance to the soma $\tilde{K}_{is}$ (by Eq. 3.27 identical to the transfer resistance $\tilde{K}_{si}$ from the soma to the dendritic site i), on the other hand, only varies by about a factor

TABLE 3.1
Transfer and Input Resistances

Location	$\tilde{K}_{ii}$	$\tilde{K}_{is}$	$\lvert\tilde{K}_{ii}(10)\rvert$	$\lvert\tilde{K}_{is}(10)\rvert$	$\lvert\tilde{K}_{ii}(1000)\rvert$	$\lvert\tilde{K}_{is}(1000)\rvert$	L
soma	16.5	16.5	14.6	14.6	1.71	1.71	0
b1	388	15.5	383	13.6	71.4	0.18	0.24
b2	751	15.2	667	13.3	99.3	0.053	0.43
a1	63.4	13.9	50.7	11.1	6.48	0.052	0.33
a2	194	12.1	156	8.43	23.4	3.3×10^{-3}	0.52
a3	342	10.5	258	6.62	30.8	0.11×10^{-3}	0.75
a4	3298	7.8	2609	4.10	216	0.053×10^{-6}	1.31
a11	178	12.4	148	8.94	30.9	5.2×10^{-3}	0.49
a12	404	11.2	335	7.53	45.2	0.30×10^{-3}	0.69

Input and transfer resistances (in megaohms) between dendritic locations and the soma of the layer 5 pyramidal cell shown in Fig. 3.7. $|\tilde{K}_{is}|$ is computed for sustained as well as for 10 and 1000 Hz sinusoidal inputs. The voltage-dependent conductances at the soma were replaced by their slope conductances, rendering the cell passive but with the same steady-state input resistance and resting potential as the active cell. This is reflected in the low-pass behavior of $|\tilde{K}_{ij}|$ which decreases with frequency. The last column lists the normalized electrotonic distance between the synapse and the soma (computed according to Eq. 3.33). Notice the dramatic uncoupling between dendritic sites and the soma for rapidly varying input. For a discussion of the parameters used see Sec. 3.4.4.

of 2 between the most proximal and the most distal sites. Remember that the somatic potential induced by the current injection is given by the product of the injected current and the transfer resistance $\tilde{K}_{is}$. This implies that the coupling between dendritic sites and the soma depends only weakly on distance for dc or slowly varying current inputs. For rapidly varying inputs, on the other hand, the coupling will effectively be zero since the distributed capacitance throughout the tree will absorb the charge before it reaches the soma. We will develop this theme further in the following section.

To derive transfer resistances between dendritic sites we can use the third property of $\tilde{K}_{ij}$ (Eq. 3.29). For instance, to obtain the transfer resistance between two points in the apical tree, say $a3$ and $a1$, we use

$$\tilde{K}_{a3,s} = \frac{\tilde{K}_{a3,a1}\tilde{K}_{a1,s}}{\tilde{K}_{a1,a1}} \tag{3.31}$$

yielding $\tilde{K}_{a3,a1} = 47.65\ M\Omega$.

3.5 Measures of Synaptic Efficiency

The introduction of the transfer impedance $\tilde{K}_{ij}(f)$, or, for stationary current input, the transfer resistance $\tilde{K}_{ij}(0) = \tilde{K}_{ij}$, allows us to characterize the voltage as well as the current attenuation between the site i of current injection and any other location in the dendritic tree, for instance, the soma s. As we will see, these are but two of a number of different measures characterizing the *efficiency*, or the *degree of coupling*, between any particular synaptic input site and the cell body where the initiation of the action potential occurs.

3.5.1 Electrotonic Distance

The simplest of all measures, yet a potentially misleading one, is an estimate of the electrotonic distance between any one location i and the soma. In an infinite cylinder or in a single finite cylinder of diameter d, the electrotonic distance between two points i and j is

$$L_{ij} = \frac{|i-j|}{\lambda} = |i-j|\left(\frac{dR_m}{4R_i}\right)^{-1/2}, \tag{3.32}$$

where $|i-j|$ is a shorthand notation to represent the physical distance between the two points and λ the space constant. This expression immediately generalizes to the frequency-dependent electrotonic distance by replacing λ with $\lambda(f)$, as in Eq. 2.36. In as far as the cell under investigation can be approximated by a single equivalent cylinder (see Sec. 3.2; Rall et al., 1992), any point along this cylinder, corresponding to one or more equivalent locations in the original tree, can be assigned a meaningful electrotonic distance, say, relative to one end of the equivalent tree. However, as discussed in Sec. 3.2, real cells rarely satisfy the conditions necessary for them to be reduced to an equivalent cylinder.

One method to estimate the "distance" between i and the soma is to compute the electrotonic lengths of all the cylinders between i and the soma and add them up. In the continuous case, we have

$$L_{is} = \int_s^i \frac{dx}{\lambda(x)} \tag{3.33}$$

where integration takes place along the direct path between the cell body and location i. In an infinite cylinder, there exists a simple exponential relationship between the electrotonic length and the voltage attenuation (Sec. 2.2.1). In all other structures, L_{is} does *not* provide a measure of the efficacy of signal transfer, since the underlying space constant λ assumes the convenient fiction of an infinite and constant cylinder. This can be seen graphically in Fig. 2.4 for the case of a single, finite cylinder. Depending on the type of boundary condition imposed, the actual voltage attenuation in a cable can be stronger (for a killed-end) or weaker (for a sealed-end boundary condition) than in an infinite cylinder with the same diameter and membrane parameters. This difference can be substantial in real trees, given the heavy load imposed by all the additional branching. Under these conditions, L_{is} seriously underestimates the attenuation experienced by dc or transient inputs on their way to the soma. For instance, the electrotonic distance between point $a4$ in the distal apical tree and the soma is 1.31 (Table 3.1), giving rise to the expectation that the attenuation from that point to the soma (assuming an infinite cylinder) should be $e^{L \cdot a4,s} = 3.7$, yet the true voltage attenuation is around 423 for sustained current inputs and higher for transient inputs. Thus, for almost any dendritic tree, L_{is} fails to even be in the ballpark of the true voltage attenuation.

3.5.2 Voltage Attenuation

One of the most common measures is the *voltage attenuation* among two sites (Rall and Rinzel, 1973), that is, the ratio of the voltage at location i to the voltage at location j,

$$A_{ij} = \frac{V_i}{V_j}. \tag{3.34}$$

Since we are dealing with passive structures without a voltage-dependent membrane that can amplify the signal, the voltage at the input site i will always be larger than the voltage anywhere else in the tree: $A_{ij} > 1$. For the general case of a sinusoidal input current $I_i(f)$ of frequency f, we have (Koch, Poggio, and Torre, 1982)

$$\tilde{A}_{ij}(f) = \frac{\tilde{K}_{ii}(f)I_i(f)}{\tilde{K}_{ij}(f)I_i(f)} = \frac{\tilde{K}_{ii}(f)}{\tilde{K}_{ij}(f)}. \tag{3.35}$$

In general $\tilde{A}_{ij}(f)$ is a complex number. As usual, if we do not explicitly express the dependency of $\tilde{A}_{ij}$ on f, we refer to the dc component for $f = 0$.

This definition does not depend on whether this current injection was caused by a synapse or by an intracellular injection. The magnitude of $\tilde{A}_{ij}(f)$ describes by how much the voltage attenuates between i and j, with large values indicating large decrements. For a fixed input site i, $\tilde{A}_{ij}$ depends only on the transfer resistance $\tilde{K}_{ij}$. Figure 3.8 illustrates this dependency for the voltage attenuation between site $a3$ in the apical tuft (Fig. 3.7) and the rest of the cell as well as the attenuation from the soma to other points. Because the ordinate is specified in units of $\tilde{K}_{ij}$, this axis is inversely proportional to $\tilde{A}_{ij}$. This type of graph is quite instructive and was first used in Rall and Rinzel (1973) to demonstrate a number of important points.

1. The attenuation from any one point toward more distal points is small. Witness this when considering the attenuation away from the soma (lower curve) or the voltage decrement from $a3$ backward, that is, toward $a4$, or in a branch away from the soma (e.g., $a11$ and $a12$). This is not surprising, since the injected current has a much easier job depolarizing high-impedance sites than low-impedance ones.

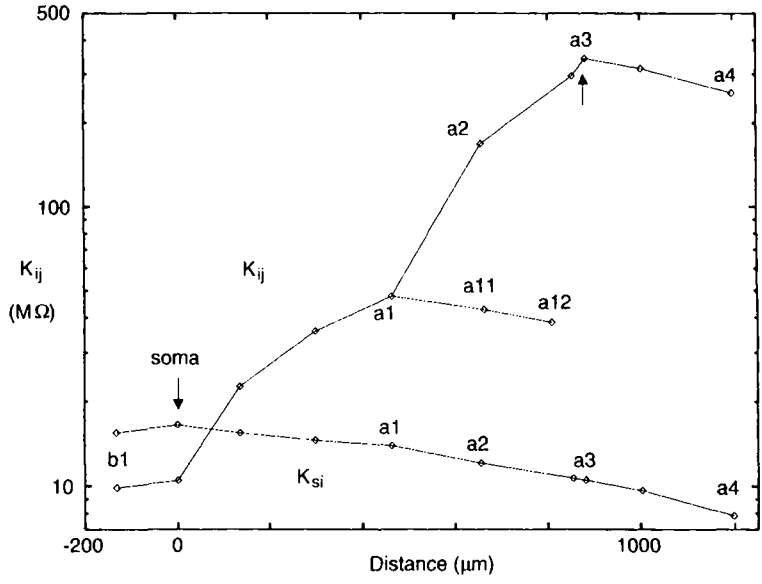

Fig. 3.8 VOLTAGE AND CHARGE ATTENUATION IN A PYRAMIDAL CELL Two curves showing the steady-state transfer resistance $\tilde{K}_{ij}$ between a site in the apical tuft (at $a3$ in Fig. 3.7) and other parts of the tree (upper trace) as well as from the soma to dendritic sites for the layer 5 pyramidal cell. The upper curve is inversely proportional to the voltage attenuation from $a3$ to other sites in the tree (Eq. 3.34), while the lower curve is inversely proportional to the charge attenuation between sites in the tree and the soma (Eq. 3.47). Note the pronounced asymmetry between large voltage attenuation but much smaller charge attenuation. The input resistances $\tilde{K}_{a3,a3}$ and $\tilde{K}_{s,s}$ are indicated by arrows.

2. On the other hand, the voltage decrement at sites on the way to the soma, a very low impedance site, is substantial. For instance, $\tilde{A}_{a3,s} = 341.68/10.46 \approx 33$: if a synaptic input to $a3$ causes a local sustained EPSP of 10 mV, the sustained somatic EPSP will be only 0.3 mV.

3. For rapid synaptic input, the actual attenuation will be larger due to the distributed capacitance that "soaks" up the high-frequency components on their way to the cell body. When the input consists of a rapid and transient current (peaking at 0.5 msec) into the dendrite at $a3$, the effective $\tilde{A}_{a3,s}$, defined as the peak of the local potential (here equal to 4.86 mV) divided by the peak somatic potential (0.051 mV), is 94, about three times larger than for sustained inputs.

4. Both sustained as well as transient voltage attenuation can be considerably larger. For the distal site $a4$, the dc attenuation alone is already 423.

5. The attenuation away from the soma is considerably smaller (Rinzel and Rall, 1974). For instance, $\tilde{A}_{s,a3}$ is only 1.6, about twentyfold less than the voltage attenuation in the reverse direction (see also the lower curve in Fig. 3.8). In fact, except for an infinite cylinder,

$$\tilde{A}_{ij} \neq \tilde{A}_{ji} . \tag{3.36}$$

This relationship appears to run counter to the symmetry of the transfer impedance, but upon closer inspection this discrepancy is resolved: Eq. 3.27 expresses symmetry

between current input and voltage output, while Eq. 3.36 expresses lack of symmetry between voltages at two different sites. The symmetry of $\tilde{K}_{a3,s}$ is expressed in the fact that the location marked *soma* on the upper curve in Fig. 3.8 has the same numerical value as the location marked $a3$ on the lower one (Rall, 1989).

The physical reason for the pronounced asymmetry between $\tilde{A}_{is}$ and $\tilde{A}_{si}$ is the large difference in input impedance between dendritic sites and the soma. While most of the current flows toward the low-impedance (or high-conductance) cell body (as expressed by Eq. 3.8), this current causes a much smaller change in the membrane potential at the soma than at high-impedance locations. This fact also explains why the voltage attenuation between $a3$ and the most distal part of the apical tree ($a4$) is comparatively minor. Given thin branches and sealed-end boundary conditions, only a very small voltage gradient exists. This is important to keep in mind when trying to understand the antidromic spread of the somatic action potential to dendritic sites.

By exploiting Eq. 3.29, we can express the voltage attenuation from i to j using any point ℓ lying on the direct path between i and j as a function of the attenuation between i and ℓ and between ℓ and j,

$$\tilde{A}_{ij} = \frac{\tilde{K}_{ii}}{\tilde{K}_{ij}} = \frac{\tilde{K}_{ii}\tilde{K}_{\ell\ell}}{\tilde{K}_{i\ell}\tilde{K}_{\ell j}} = \left(\frac{\tilde{K}_{ii}}{\tilde{K}_{i\ell}}\right)\left(\frac{\tilde{K}_{\ell\ell}}{\tilde{K}_{\ell j}}\right) = \tilde{A}_{i\ell}\tilde{A}_{\ell j}\,. \tag{3.37}$$

This property allows us to introduce a sort of pseudo *attenuation metric*. Following Zador (1993), Zador, Agmon-Snir, and Segev (1995) and Brown et al., (1992), we define the *log attenuation* as

$$\tilde{L}^{v}_{ij}(f) = \ln|\tilde{A}_{ij}(f)| \tag{3.38}$$

using the natural logarithm. Note that to differentiate this dimensionless variable from the electrotonic distance, it carries a superscript. Because $|\tilde{A}_{ij}| \geq 1$,

$$\tilde{L}^{v}_{ij} \geq 0 \tag{3.39}$$

as expected for a distance. We now make use of Eq. 3.37 and have for any point ℓ on the direct path from i to j,

$$\tilde{L}^{v}_{ij} = \tilde{L}^{v}_{i\ell} + \tilde{L}^{v}_{\ell j}\,. \tag{3.40}$$

Additivity constitutes an elegant feature of $\tilde{L}^{v}_{ij}$, rendering it somewhat similar to a distance measure. Note that $\tilde{L}^{v}_{ij}$ is not a true metric, since symmetry does not hold due to the asymmetry in the voltage attenuation,

$$\tilde{L}^{v}_{ij} \neq \tilde{L}^{v}_{ji}\,. \tag{3.41}$$

In the special case of an infinite cylinder, it follows from Eq. 3.23 that

$$\tilde{A}_{ij} = \tilde{A}_{ji} = e^{+|i-j|/\lambda} \tag{3.42}$$

and, therefore,

$$\tilde{L}^{v}_{ij} = \tilde{L}^{v}_{ji} = \frac{|i-j|}{\lambda}\,. \tag{3.43}$$

Because the logarithm of the voltage attenuation between two points in an infinite cable equals the electrotonic distance between them, $\tilde{L}^{v}_{ij}$ can be viewed as a generalization of the

traditional notion of electrotonic distance to arbitrary cable structures (Zador, Agmon-Snir, and Segev, 1995).

While voltage attenuation has been and continues to be a popular measure of synaptic efficiency, it should not be forgotten that it represents a relative measure. And whether or not the cell spikes by exceeding a threshold voltage depends on the absolute amplitude of the somatic EPSP and not on the relative ratio of voltages.

3.5.3 Charge Attenuation

Another measure of synaptic efficiency is the ratio of the charge transferred across the membrane at the location of the input i to the charge reaching location j (Koch, Poggio, and Torre, 1982). The total charge transferred at i due to the current $I_i(t)$ is

$$Q_i = \int_{-\infty}^{+\infty} I_i(t)dt\,. \tag{3.44}$$

This equals the steady-state value of the Fourier transform of the current

$$\tilde{I}_i(f=0) = \int_{-\infty}^{+\infty} I_i(t)dt = Q_i\,. \tag{3.45}$$

The charge transferred across the membrane at j is

$$Q_j = \int_{-\infty}^{+\infty} I_j(t)dt = \tilde{I}_j = \frac{\tilde{K}_{ij}}{\tilde{K}_{jj}}\,\tilde{I}_i\,. \tag{3.46}$$

The *charge attenuation* from i to j, defined by analogy to the voltage attenuation, is

$$\frac{Q_i}{Q_j} = \frac{\tilde{K}_{jj}}{\tilde{K}_{ij}} = \tilde{A}_{ji}\,. \tag{3.47}$$

Or, the charge attenuation from i to j is identical to the voltage attenuation in the reverse direction (for this reason, Zador, Agmon-Snir, and Segev, 1995, also refer to the charge attenuation as *outward going attenuation*). This allows us to use the lower trace in Fig. 3.8, which is proportional to the voltage decrement $\tilde{A}_{si}$ from the soma to dendritic sites, as an indicator for the charge attenuation between these sites and the soma. For the parameters used in this model, $\tilde{A}_{si}$ is usually below 2, even for the most distal sites in the layer 1 dendrites. It should not be forgotten that $\tilde{A}_{si}$ is a relative measure and does not tell us anything about the absolute amount of charge transferred from the synapse i to the cell body. Due to the equivalence of charge attenuation and inverse voltage attenuation, the logarithmic transform of Eq. 3.38 can be used to define a pseudodistance.

The charge attenuation has, in contrast to the voltage attenuation, the distinction that it is independent of the time course of the current $I_i(t)$. It simply provides an index of the relative amount of charge reaching the cell body. Of course, this measure also stipulates that the period of integration extends to infinity, which means in practice several time constants, until all ions have charged and discharged the neuronal membrane between i and the soma.

It is also possible to define the *current attenuation* as the ratio of the input current flowing at location i and the current flowing across the neuronal membrane at j,

$$\frac{I_i(f)}{I_j(f)} = \frac{\tilde{K}_{jj}(f)}{\tilde{K}_{ij}(f)} = \tilde{A}_{ji}(f)\,. \tag{3.48}$$

This implies that the steady-state current attenuation between i and j is identical to the charge attenuation between these two sites. It is important to understand here that the current I_j does *not* correspond to the intracellular current that flows from i to j. Rather, I_j is the current that needs to be injected across the membrane at location j in order to change the potential at j by the same amount as the current i does (namely, by $\tilde{K}_{ij} I_i$).

3.5.4 Graphical Morphoelectrotonic Transforms

It is more and more common that the detailed, three-dimensional morphology of reconstructed neurons is available in computer readable form. It therefore becomes possible to reexpress the geometry of a specific tree using different measures, for instance, the electrotonic length, the log attenuation pseudodistance measure, or the dendritic delay. As a group, these transforms, introduced by Zador (1993; Zador and co-workers 1992, 1995; see also Bernander, Douglas, and Koch, 1992), have been called *morphoelectrotonic transforms* (METs). In a MET, the anatomical length of each dendritic cable segment is replaced by one of these various measures, while the diameter and the orientation of the segment are preserved. In this way, different aspects of the electrotonic structure of the cell can be directly visualized. Color can be used as a further visual aid to identify corresponding points between different METs and the original anatomy.

Figure 3.9 illustrates these procedures without the use of color. The original anatomy, derived from projecting the three-dimensional digitized coordinates of the tree onto the image plane, is shown in (A). In (B), the anatomical length of each compartment is replaced by its electrotonic length. Therefore, the distance between a point i and the soma corresponds to L_{is} (Eq. 3.33). In particular, the thin basal and distal apical dendrites are accentuated at the cost of the thick apical trunk, since thinner cables have shorter space constants and are therefore electrotonically longer. The electrotonic length does *not* correspond to the strength of coupling between i and the cell body, since the use of L is conditioned upon the space constant λ that is defined for an infinite cylinder. With the total electrotonic length of the cell being on the order of one λ, we would expect that stationary signals from the periphery decay by a factor of $1/e$, while their actual decay is more substantial (Table 3.1).

The log transform of the voltage attenuation from the dendritic tree to the soma ($\tilde{L}^v_{is}$; Fig. 3.9C) and from the soma to dendritic sites ($\tilde{L}^v_{si}$; Fig. 3.9D) emphasizes the large differences (about a factor of 10) between incoming and outgoing voltage decrement. The outgoing voltage attenuation MET in Fig. 3.9D corresponds to the logarithmic transform of the charge attenuation from sites in the dendritic tree to the soma. The transforms are functional, in the sense that the voltage transfer can be directly read off from the figure. (This is a consequence of the additivity of the $\tilde{L}^v$ measure, as expressed in Eq. 3.40.) For instance, the voltage attenuation from $b2$ at the tip of a basal dendrite is $e^{3.9} \approx 50$, while the charge injected at the same site will only attenuate by $e^{0.08} \approx 1.09$. This also means that a long-lasting hyperpolarization at the cell body of 10 mV will hyperpolarize the entire basal tree, an area that accounts for 62% of the cell's membrane area, by at least 9.5 mV. Since the most distal sites in layer 1 of the apical tree have an $\tilde{A}_{si}$ value of about 2.1, even these parts will be hyperpolarized by about 4.8 mV.

Zador, Agmon-Snir, and Segev (1995) offer another interpretation of $\tilde{L}^v_{si}$. A frequently asked question relates to the *cost* of moving a synapse from the soma to a particular location i in the tree. Assuming that the synaptic input can be treated as a current and is identical to I_0 at both locations, the voltage induced by the somatic location is given by $\tilde{K}_{ss} I_0$, while the somatic potential in response to the dendritic input is $\tilde{K}_{is} I_0$. The ratio of the

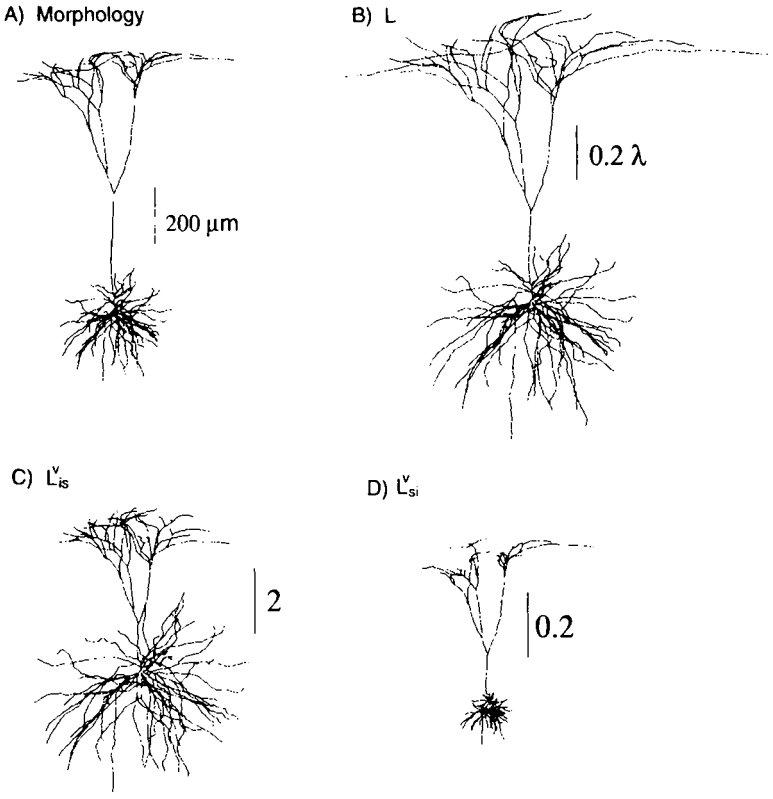

Fig. 3.9 MORPHOELECTROTONIC TRANSFORMS Graphical means of visualizing different measures of synaptic efficiency using morphoelectrotonic transforms (METs) (Zador, 1993). **(A)** Two-dimensional projection of the layer 5 pyramidal cell (see also Fig. 3.7). **(B)** The physical length ℓ of each dendritic compartment is replaced by the electrotonic length $L = \ell/\lambda$, while the orientation of the compartment remains constant. In an infinite cable, the voltage attenuation between two sites a distance L apart is e^{-L}. But because the electrical structure of the dendritic tree is quite distinct from that of an infinite cable, the voltage decay from dendritic sites to the soma is much larger than indicated by this measure. **(C), (D)** METs corresponding to the logarithmic voltage attenuation from sites i in the tree toward the soma, $\tilde{L}^v_{is} = \ln|\tilde{A}_{is}|$, and from the soma to the tree, $\tilde{L}^v_{si} = \ln|\tilde{A}_{si}|$, for stationary input. The latter measure is equivalent to the charge attenuation, that is, to the ratio of the charge injected at i to the charge reaching the soma (after integrating for a time that is long compared to τ_m). Notice the very different scales (corresponding to the distance over which the signal attenuates by a factor of $e^{2.0} = 7.39$ and $e^{0.2} = 1.22$, respectively), attesting to the fact that neurons are very compact from the point of view of charge but very dispersed from the point of view of voltage attenuation. These METs provide a snapshot of the cell's electroanatomy for a particular configuration of electrical parameters.

membrane potential induced by the somatic input to the EPSP induced by the dendritic input is $\tilde{K}_{ss}/\tilde{K}_{is} = \tilde{A}_{si}$. As an example, moving a sustained current injection from the soma to site $a4$ in the distal apical tree, reduces the effect of this input by only a factor of 2.1. Of course, for rapidly varying input, the cost of moving to the dendrites can be substantially higher (for the same synapse, a factor of about 4 for input changing at the 10-Hz scale and a factor of 20 million for input varying at the kilohertz scale).

If transient input is used at the soma, the outgoing voltage attenuation is much larger. This is demonstrated in Fig. 3.10 for a sinusoidal input of 1000 Hz. This frequency corresponds

approximately to the inverse of the width of a typical action potential and provides us with some intuition for how far the very rapid portion of a somatic action potential will propagate into a passive tree (a phenomenon known as *antidromic spike invasion*). While the somatic potential in response to current input at a distal, apical site ($a4$ in Fig. 3.7) is 423 times smaller than the dendrite EPSP for stationary inputs (but only losing half of the injected charge in the process) and 630 times smaller for a 10-Hz sinusoidal, it is attenuated by a staggering factor of 4 billion for a 1000-Hz sinusoidal input. In other words, without dramatic amplification by active processes, a distal high-frequency input has no chance of ever influencing anything occurring close to the soma (see Chap. 19).

A further feature of METs is that they reflect the momentary state of the cell, a state that can be modulated by any number of different events in the brain. For instance, as discussed in Sec. 18.3.3, varying the synaptic background—corresponding to effectively varying the membrane resistance R_m—modulates the electrotonic geometry of the cell by changing the L_{is} or $\tilde{L}_{is}^{v}$ (see Fig. 18.6). Or if some brainstem afferent releases a neuromodulator, such as noradrenaline or acetylcholine, onto part of the cell, its electroanatomy can shrink or grow, reflecting the corresponding change in the efficiency of synaptic inputs.

Figure 3.11, from Zador, Agmon-Snir and Segev (1995), provides a graphical comparison of $\tilde{L}_{si}^{v}$ for four different neurons with identical, albeit passive, membrane properties. The differences between them are dramatic. Given the large diameter of the Purkinje cell dendrites, almost no charge attenuation occurs for sustained current inputs. The electrotonic behavior of the layer 2/3 pyramidal cell is very similar to the behavior of the basal tree of the layer 5 cell. Finally, the apical tree of the hippocampal pyramidal cell sprouts into a long, central stalk across which substantial charge attenuation occurs.

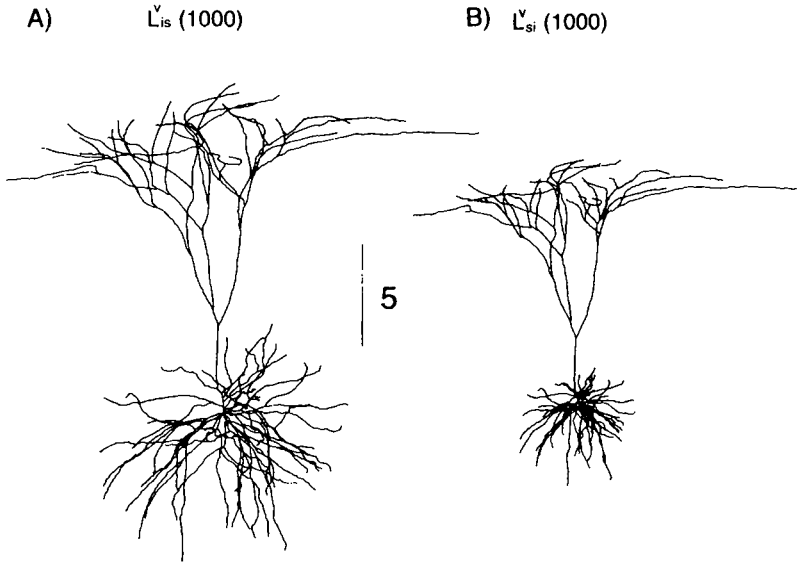

Fig. 3.10 Dynamic Morphoelectrotonic Transforms **(A)** Logarithm of the voltage attenuation, $\ln|\tilde{A}_{is}(f)| = \tilde{L}_{is}^{v}(f)$ for a 1000 Hz input. For such transient input, the most distal site is 27 units away from the cell body (for stationary inputs, the corresponding distance is 6.7; see Fig. 3.9C). **(B)** Logarithm of the voltage attention $\tilde{L}_{si}^{v}(f)$ from the soma to dendritic sites for the same 1000-Hz input. This frequency has been choosen to demonstrate how far the fast components in a somatic action potential (with an approximate width of 1 msec) can propagate back into the dendritic tree.

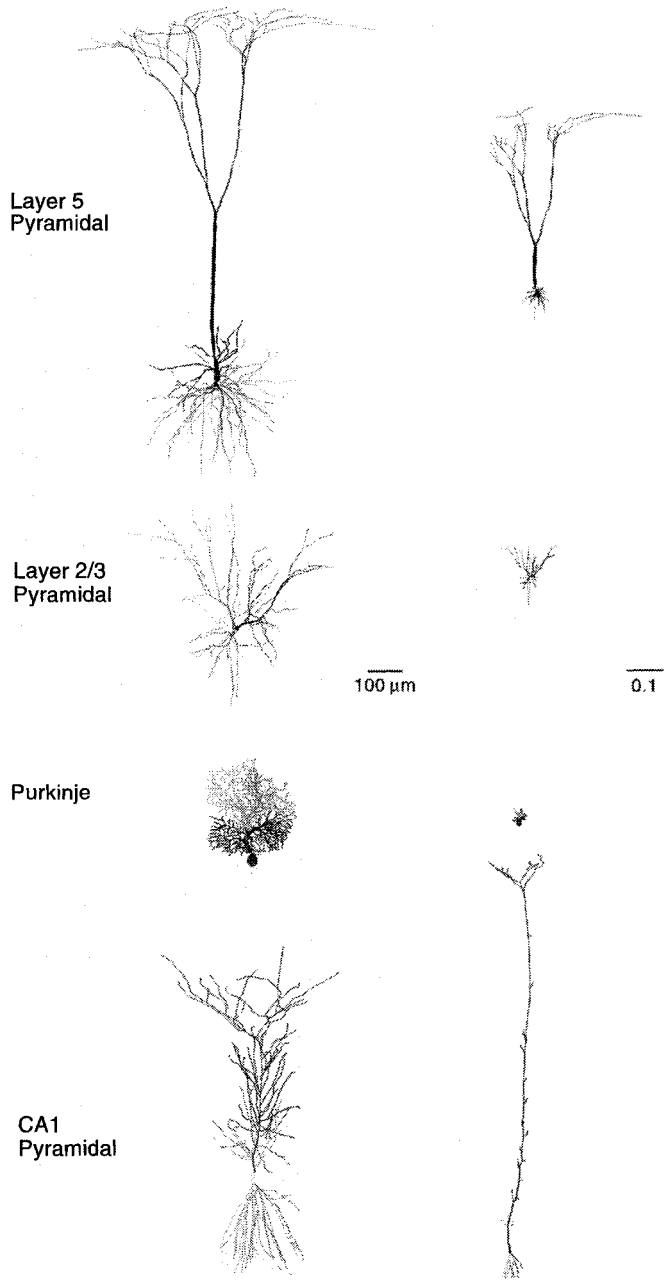

Fig. 3.11 MORPHOELECTROTONIC TRANSFORMS FOR DIFFERENT CELL TYPES Comparison of the logarithm of the charge attenuation—corresponding to the log-voltage attentuation from the soma to dendritic sites for stationary inputs—for four different neurons: the layer 5 neocortical pyramidal cell used throughout, a layer 2/3 neocortical pyramidal cell, a Purkinje cell from the cerebellum of a guinea pig, and a CA1 pyramidal cell from rat hippocampus (Zador, Agmon-Snir, and Segev, 1995). The left column corresponds to the morphology and the right one to $\tilde{L}_{si}^{v}(0)$. The scale bar, indicating the distance over which the voltage attenuates by $e^{0.1} \approx 1.1$, applies to all cells. To facilitate comparison, all neurons are passive with identical membrane parameters ($R_m = 100,000\,\Omega\cdot\text{cm}^2$, $R_i = 100\,\Omega\cdot\text{cm}$). Reprinted in modified form by permission from Zador, Agmon-Snir, and Segev (1995).

3.6 Signal Delays in Dendritic Trees

We discussed in Sec. 2.3 transient inputs and their effect on the voltage in single cables. The most important parameter regulating how fast the membrane potential equilibrates is the neuronal *time constant* τ_m. But how is τ_m measured experimentally in dendritic trees? Following Agmon-Snir and Segev (1993), we also introduced a new measure of neuronal delay in terms of the difference between the centroid or center of mass of the current input and the voltage signal. How do these definitions fare in spatially extended structures?

3.6.1 Experimental Determination of τ_m

A general property of the voltage response to current input into an arbitrary complex, passive cable structure (whether a single finite cylinder or a large dendritic tree) with uniform electrical parameters throughout the tree is that it can always be expressed as an infinite sum of exponentials (Rall, 1969a; for more details, consult Appendix C),

$$V(x,t) = V_\infty(x) + B_0 e^{-t/\tau_0} + B_1 e^{-t/\tau_1} + B_2 e^{-t/\tau_2} + \cdots, \tag{3.49}$$

where the B_i's depend both on the initial conditions and on x, and V_∞ captures the steady-state components of the voltage. The τ_i's can be thought of as *equalizing constants* that govern the rapid flow of current (and the reduction of voltage differences) between different regions of the cable. They are independent of the site of the current input, the site of recording, or the initial voltage distribution in the tree. In general, solving for these τ_i's involves extracting the root of a recursively defined transcendental equation. (For more recent work on this, see Holmes, Segev, and Rall, 1992; Major, Evans, and Jack, 1993a.)

Several important points need to be mentioned here. First, in a tree with uniform membrane properties with sealed ends (and without a shunt or a voltage clamp) the slowest time constant τ_0 is always equal to the membrane time constant, $\tau_0 = \tau_m = R_m C_m$. Second, all time constants scale with the membrane capacitance C_m. Third, introducing a shunt conductance at the soma—mimicking the effect of an intracellular electrode—reduces all the time constants, including τ_0. In other words, under realistic experimental conditions, the measured slowest τ_0 represents a lower bound on the actual value of τ_m. As evident in Eq. 2.40, these τ_i's have a particularly pleasing and simple interpretation for a single finite passive cable with sealed-end boundaries.

Direct measurements of τ_m in neurons depended on the development of the intracellular electrode, introduced by Graham and Gerard (1946) for muscles and first applied to central mammalian neurons (spinal motoneurons) by Woodbury and Patton (1952) and Brock, Coombs, and Eccles (1952). These early studies neglected the cable properties of the dendrites and estimated $\tau_m = 2$ msec. A common numerical technique for extracting time constants involves the *peeling* of low-order exponentials from a semilogarithmic plot of the voltage decay (Rall, 1969a,b; see Fig. 3.12). It was first applied to the problem of extracting time constants in α motoneurons by Burke and Ten Bruggencate (1971).

They estimated that τ_m ranges from 5 to 7 msec. Averaging over 50 voltage transients allowed them to determine not only $\tau_0 = \tau_m$ but also the next slowest time constant τ_1, which they calculated to be around 1 msec. Assuming that the dendritic tree of the motoneuron can be reduced to a single, equivalent cable, allowed Burke and Ten Bruggencate (1971) to exploit Eq. 2.42 to estimate the electrotonic length at around 1.5.

Experimentally, τ_m can be determined by injecting a brief current pulse into the soma and recording the voltage response at the same point. Long current steps tend to activate

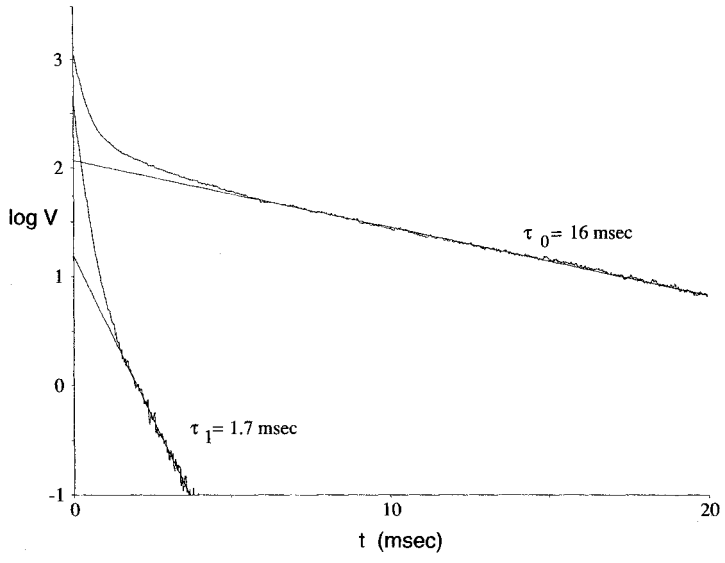

Fig. 3.12 ESTIMATING THE FIRST TWO TIME CONSTANTS Peeling procedure to assess the time constants of voltage decay in response to a small and short current pulse. The data shown here were obtained by recording from a pyramidal cell located in the upper layers in the frontal cortex of the guinea pig. The voltage response is shown as a logarithmic function of time. Due to the nonisopotential nature of the dendrites, the voltage decays initially rapidly; the slowest time constant $\tau_0 = \tau_m$ is only evident toward the tail of the response, with $\tau_0 = 16$ msec. Peeling it away reveals the second slowest time constant $\tau_1 = 1.7$ msec. The recordings were carried out at the cell's resting potential of −65 mV in the laboratory of Yosef Yarom. Reprinted by permission from Koch, Rapp, and Segev (1996).

voltage-dependent components (e.g., the over- and undershoot dealt with in detail by Ito and Oshima, 1965) that severely interfere with the measurement of the passive time constant. In a linear system, the response to a current pulse is given by the temporal derivative of the response to a step. Because the derivative of Eq. 3.49 still leaves an infinite number of exponential terms with the slowest term decaying as e^{-t/τ_m}, the peeling method is also applicable to the derivative of $V(t)$ in Eq. 3.49 with the advantage that the steady-state component of the voltage disappears. The slope of the tail of the decaying phase of V_m, when plotted on a semilogarithmic scale, is $-1/\tau_m$. Figure 3.12 illustrates this procedure for a voltage transient in a guinea pig neocortical pyramidal cell, showing how the voltage gradients over the cell surface equalize after about 6–8 msec; from this time on, the voltage decays exponentially. The slowest time constant $\tau_0 = 16$ msec corresponds to the inverse of the slope at the tail end of the voltage distribution (see also Kim and Connors, 1993). Subtracting this component from the original voltage curve gives rise to a new transient (noisy curve at bottom) whose tail can now again be fitted with a straight line whose slope is $-1/\tau_1$. In this case $\tau_1 = 1.7$ msec. If we assume that the membrane of this cell is uniform and that the intracellular electrode did not cause a significant shunt (injury), $\tau_0 = \tau_m$.

It is important to emphasize that the quality of the electrical recording depends to a large extent on the tightness of the resistive *seal* around the electrode. During the impalement of the neuronal membrane, the intracellular electrode frequently rips a large hole in the membrane, allowing ions to flow through, thereby seriously compromising the quality of the recording. The introduction of the whole-cell recording of *in vitro* cells and the perforated patch clamp technique (Edwards et al., 1989; Spruston and Johnston, 1992) has dramatically

improved the situation with an effective electrode shunt on the order of 0.1 nS. Indeed, over the last four decades the estimate for τ_m in central neurons has grown significantly. In the 1950s it was assumed to be only a few milliseconds. With improved averaging and recording techniques, the recent estimates of τ_m from intracellular recordings range from 10 to 40 msec for the major types of central neurons. (See Fleshman, Segev, and Burke, 1988 and Clements and Redman, 1989, for α motoneurons, Brown, Fricke, and Perkel, 1981, for hippocampal neurons, Nitzan, Segev, and Yarom, 1990, for vagal motoneurons and Rapp, Segev, and Yarom, 1994, for cerebellar Purkinje cells.) With tight-seal whole-cell recordings, the estimates are growing even further and are approaching 100 msec in slice preparations (e.g., Andersen, Raastad and Storm 1990 found time constants ranging from 50 to 140 msec in the hippocampus; Major et al., 1994 report an average value of 93 msec in CA3 pyramidal cells; see also Spruston, Jaffe, and Johnston, 1994). A notable exception to such high values is the 2-msec time constant in slices in the avian cochlear nucleus responsible for processing high-fidelity sound information, measured by using whole-cell recording with tight seal (Reyes, Rubel, and Spain, 1994). We conclude this section by noting that τ_m estimates depend heavily on the composition of the physiological solution during the experiment. Adding specific blockers to the solution, as is frequently done (e.g., caesium ions to block K^+-dependent rectification or blockers of NMDA-dependent channels), directly affects (typically increases) estimates of τ_m.

3.6.2 Local and Propagation Delays in Dendritic Trees

The problem with the standard definition of τ_m is twofold. Firstly, because τ_m is a property of the membrane it does not take into consideration the effect of the neuronal structure on the dynamics of the membrane potential at the input site (which can be the soma, a thin dendrite, or an elongated spine). Secondly, τ does not inform us about how rapidly the membrane can respond to more physiological input than a current pulse or step. Both problems were addressed by Agmon-Snir and Segev (1993) (see also Zador, Agmon-Snir, and Segev, 1995). In Chap. 2, we defined the *transfer delay* D_{ij} to be the difference in the centroid of the induced voltage at location j and the centroid of the current flowing at i (Eq. 2.45) and the *input delay* D_{ii} as the difference between the centroids of the local voltage and the injected current at the same location (Eq. 2.46). For an infinite cable, the transfer delay $D_{ij} = (1 + |i - j|/\lambda)\tau_m/2$ (Eq. 3.50).

The center of mass method can be applied to calculate analytically the local delay at any point in an arbitrary dendritic tree. Figure 3.13 illustrates a few delays arising in the pyramidal cell for fast current injections of the form expected during activation of fast voltage-independent synaptic input. The time course follows that of the α function introduced in Eq. 1.21,

$$I_{\text{syn}}(t) = \frac{I_{\text{peak}}}{t_{\text{peak}}} t e^{1-t/t_{\text{peak}}} . \tag{3.50}$$

(We here approximate the synaptic input by a current source.) The current attains its peak value I_{peak} at $t = t_{\text{peak}}$. Values for the latter are in the 0.25–1-msec range, depending on the exact circumstances (for more details see Sec. 4.6). The centroid of the current is located at $2t_{\text{peak}}$.

The local delay D_{ii} reflects the RC properties of the local membrane as well as the electrotonic structure of the cell as seen from location i. It is maximal (and equal to τ_m) for the membrane patch case (Eq. 2.48), since here the input current can only discharge through

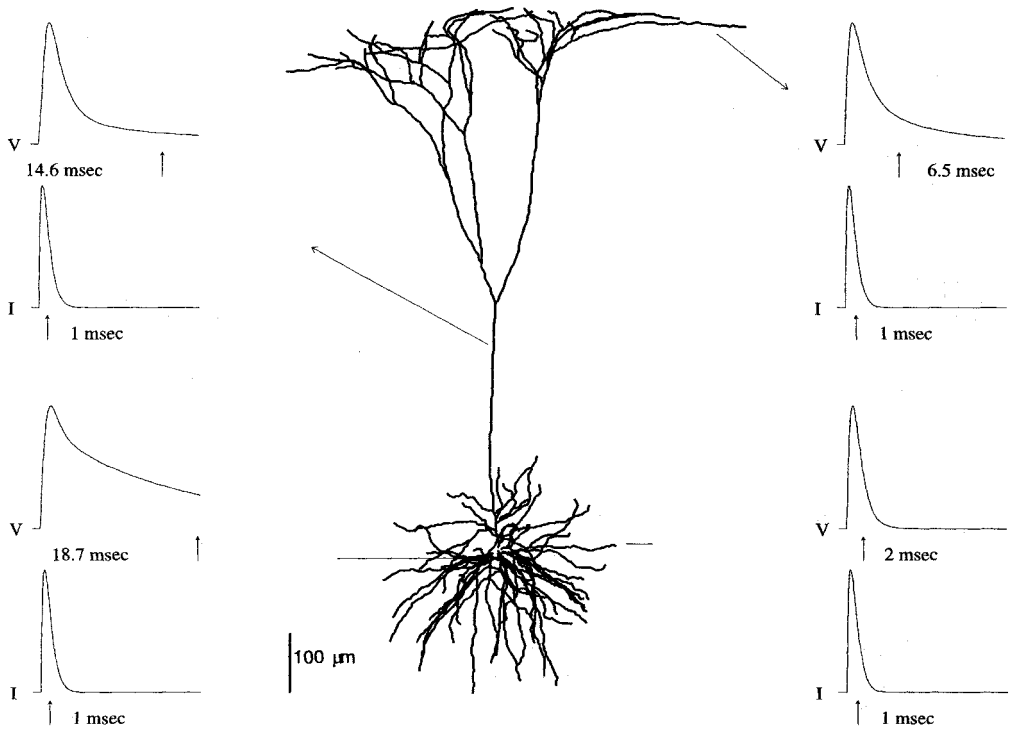

Fig. 3.13 Local Delay Four examples of the local delay D_{ii} defined as the difference between the centroid of the local voltage (upper curves in the four panels) and the centroid of the local current injection that gave rise to this depolarization (lower curves in the four panels) for the layer 5 pyramidal cell from neocortex. D_{ii} reflects the contribution of the geometry of the cable structure to the voltage dynamics and is independent of the waveform of the current input. The input current is given by Eq. 3.50 with $t_{peak} = 0.5$ msec and a centroid at 1 msec (the centroids are marked with arrows). At the soma (lower left) $D_{ii} = 17.7$ msec $\approx \tau_m$, while at distal sites, such as a layer 1 apical dendrite (upper right) or the tip of a layer 5 basal dendrite (lower right), D_{ii} can be much faster than τ_m. $R_m = 20,000\ \Omega \cdot \text{cm}^2$ and $C_m = 1\ \mu\text{F/cm}^2$throughout the cell. The amplitude of all responses have been normalized and shifted by 0.5 msec to the right. Reprinted by permission from Koch, Rapp, and Segev (1996).

one pathway. In an infinite cable, $D_{ii} = \tau_m/2$, since current can flow through membrane resistance as well as through the intracellular resistivity (Fig. 2.11). Adding additional current sinks, in the form of a complex and highly branched dendritic tree, further reduces D_{ii}.

Because the soma is relatively large (with a radius of 20 μm), D_{ii} at the soma is not very far from that of an isopotential membrane patch, $D_{ii} = 17.7$ msec $\approx \tau_m$ (lower left in Fig. 3.13). For distal sites in the layer 5 pyramidal cell, $D_{ii} \approx \tau_m/10$ or less (upper and lower right-hand panels in Fig. 3.13), while for dendritic spines $D_{ii} \approx \tau_m/20$ (not shown). Such small values of D_{ii} go hand in hand with a narrow (brief) voltage transient at the input sites (Rinzel and Rall, 1974). Indeed, distal dendritic arbors, in particular the many fine branches of the basal tree, provide for multiple sites with a very brief (compared to τ_m) and local voltage response, provided the input is also brief. This will be taken up in more detail further below as well as in Chap. 19.

The transfer delay between i and j really includes two components, the time it takes for the current input to depolarize (or hyperpolarize) the local membrane (that is, D_{ii}) and the

time it takes the centroid of the local potential to propagate to j. Accordingly, Agmon-Snir and Segev (1993) define the *propagation delay* as

$$P_{ij} = \hat{t}_j^V - \hat{t}_i^V = D_{ij} - D_{ii} . \tag{3.51}$$

This measure has a number of similarities with the log attenuation $\tilde{L}_{ij}^v$ measure defined in Sec. 3.5.2. In particular, it is not symmetric,

$$P_{ij} \neq P_{ji}, \tag{3.52}$$

but it is additive for all locations ℓ on the direct path between locations i and j:

$$P_{ij} = P_{i\ell} + P_{\ell j}. \tag{3.53}$$

This last property allows us to compute the morphoelectrotonic transforms for P_{ij} just like we did for the log voltage attenuation measure (Zador, Agmon-Snir, and Segev, 1995). Before we discuss the functional significance of these different delays in realistic dendritic trees, we would like to note the analogies between input and transfer resistances and input and transfer delays. Both sets of variables are defined as quantities relating current at location i to voltage at location i or j and both obey the same symmetry relationships.

The propagation delay P_{is} from a dendritic site i to the soma s is obtained by subtracting the local delay at i from the transfer delay from i to the soma, reflecting the actual propagation time of the voltage centroid from the input site to the soma. We can, of course, also define a propagation delay from the soma to dendritic sites P_{si} (Agmon-Snir and Segev call this the *net dendritic delay*, to indicate that P_{si} measures the "cost" in terms of delay that results from placing the input at the dendritic site i rather than at the cell body). This measure turns out to be the most useful of all. Reverting back to the definitions of P_{ij} and D_{ij} given in Sec. 2.4, we have

$$P_{si} = D_{si} - D_{ss} = D_{is} - D_{ss} \tag{3.54}$$

that is, we can think of P_{si} as the difference between the voltage response at i to a somatic input and the voltage response at the soma to a somatic input. Because the decay phases of both EPSPs are relatively similar (being primarily dictated by the properties of the large cell body), P_{si} reflects differences in the rising phases of the EPSPs. In this sense, P_{si} has similar values and can be interpreted as the time delay between the peak of the local EPSP and the peak in the somatic EPSP. Figure 3.14 illustrates the MET of the propagation delay P_{si} for the layer 5 pyramidal cell devoid of synaptic background activity. An extreme case is shown for which R_m is reduced tenfold. In an infinite cable, this leads to a $\sqrt{10}$ reduction in the propagation delay (Eq. 2.52). In fact, the scaling is more complex for a distributed dendritic tree. It takes the centroid of the somatic EPSP between 1 and 2 msec to propagate to the tips of the basal dendrites (and proximal apical dendrites) independent of R_m, while P_{si} to the tip of a typical apical dendrite decreases by about a factor of 2 to about 10–15 msec.

The *outward going propagation delay* P_{si} has another interesting interpretation. Using Eq. 2.51, we have

$$P_{si} = D_{is} - D_{ss} = (\hat{t}_s^V - \hat{t}_i^I) - (\hat{t}_s^V - \hat{t}_s^I) = \hat{t}_s^I - \hat{t}_i^I . \tag{3.55}$$

In other words, it corresponds to the difference between the centroids of the current at the soma and at site i.

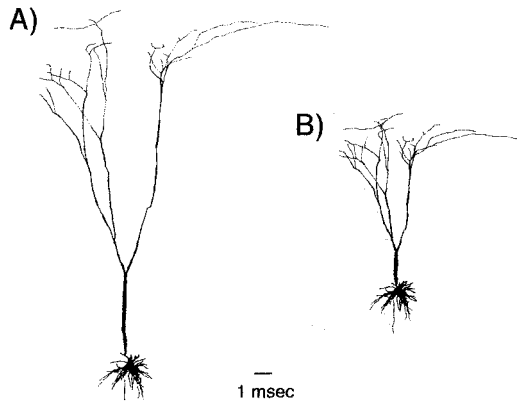

Fig. 3.14 PROPAGATION DELAY Morphoelectrotonic transform (MET) for the outward going propagation delay P_{si} from the soma to dendritic sites (Agmon-Snir and Segev, 1993) computed for the layer 5 pyramidal cell with **(A)** a very high value of $R_m = 100,000\ \Omega \cdot \text{cm}^2$ or **(B)** a 10 times reduced value of $10,000\ \Omega \cdot \text{cm}^2$. P_{si} corresponds to the effective delay between the peak of the local EPSP at i and the somatic EPSP. Changing R_m by a factor of 10 should reduce the propagation by $\sqrt{10}$ for an infinite cable, while the effect is much less in a distributed tree. P_{si} to the main branch point of the apical tree is 6 msec for the high and 2.5 msec for the low R_m value.

3.6.3 Dependence of Fast Synaptic Inputs on Cable Parameters

While the dynamics of the membrane potential in response to a slowly varying input current is dictated by τ_m, this is most emphatically not the case for rapid inputs (Segev and Parnas, 1983). For fast synapses onto thin dendrites, the rise time as well as the initial decay of the associated postsynaptic potential is almost completely independent of R_m and is primarily limited by the dynamics of the synaptic current, that is, ultimately by how fast the underlying ionic channels open and close (e.g., D_{ii} for distal dendritic sites in Fig. 3.13).

Let us consider how three aspects of the excitatory postsynaptic potential depend on the three cable parameters, R_m, C_m, and R_i: (1) its rise time or rate of depolarization, (2) its peak potential, and (3) its rate of repolarization.

For a fast synaptic input, the rate of depolarization in an infinite cable of diameter d is limited by the temporal derivative of the membrane potential in response to a current step of amplitude I_0. Using Eq. 2.33 and recalling that the derivative of the error function is $2e^{-x^2}/\sqrt{\pi}$ yields

$$\frac{dV_{\text{step}}(0,t)}{dt} = \frac{R_i^{1/2} I_0}{(\pi d)^{3/2} C_m^{1/2}} \frac{e^{-t/\tau_m}}{t^{1/2}}. \tag{3.56}$$

At very short times when the exponential term can be developed in a Taylor series, the derivative behaves as $\text{const}/\sqrt{t}$, where const depends on R_i, I_0, and C_m, but *not* on R_m. What happens is that initially the injected current primarily charges up the membrane capacitance at the site of current injection as well as at neighboring locations (via the axial resistance R_i). The larger the R_i or the smaller the C_m, the faster the voltage will change. It is only the slow components of the decay that are affected by low-pass filtering, as demonstrated graphically in Fig. 3.15. Here the dendritic potential in response to a single depolarizing current input (Eq. 3.50) in the pyramidal cell is computed for

$R_m = 10{,}000\,\Omega \cdot \text{cm}^2$ and $R = 100{,}000\,\Omega \cdot \text{cm}^2$. While the dc input and transfer resistances are affected appropriately, almost no effect on the rise time is evident.

Surprisingly, both the peak depolarization as well as the initial phase of the repolarization of the voltage change are not affected by the tenfold change in R_m. This surprising behavior is only seen in thin dendrites and not at the soma: because of the limited membrane area, all of the injected current charges up the associated capacitance. The rapid repolarization

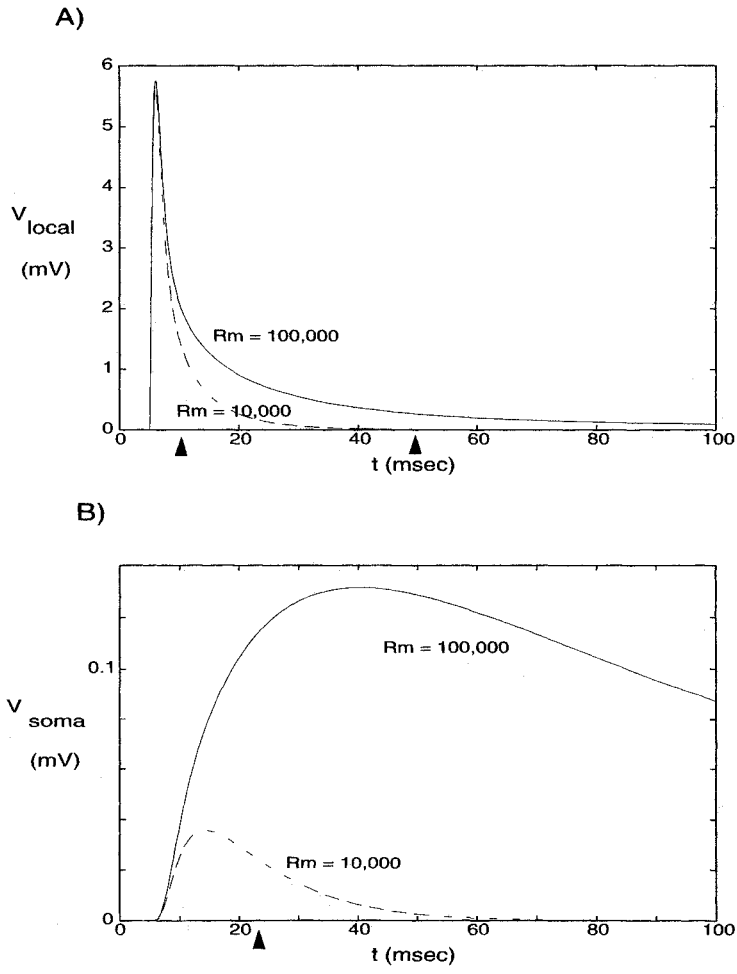

Fig. 3.15 Weak Dependence of Fast Dendritic EPSP on R_m **(A)** Dendritic and **(B)** somatic synaptic potentials in response to a single fast excitatory synapse activated 5 msec into the simulation and located at $a3$ in the distal apical tree of the layer 5 pyramidal cell (see Fig. 3.7) for two different values of R_m (in units of $\Omega \cdot \text{cm}^2$). The current peaks 0.5 msec after onset and is over within 2 msec. This is so fast compared to the membrane time constant of either 10 or 100 msec that the rising phase as well as the peak dendritic response is more or less independent of R_m. Indeed, because the input is so fast compared to the time constant of the dendrite, the local voltage response approximates the impulse response. Due to the low-pass filtering between the synapse and the soma, the somatic potential is strongly affected by the decrease in electrotonic distance and the increase in τ_m. This shows the fallacy of using τ_m as an indicator for how rapidly the membrane can respond to synaptic input. Arrows point to the location of the centroids.

occurs because the capacitances outside the immediate neighborhood of the site of current injection (which includes the distant cell body) soak up the charge. The synaptic current is so rapid that all of this takes place with only little involvement of the membrane resistance. Because of the much larger capacitance present at the soma, the dendrites branching from the cell body fail to provide any substantive capacitive sink and repolarization is much slower (witness the decay of the somatic and the dendritic voltages in Fig. 3.13).

Rall (1964) first observed that this capacitive effect allows for faster than exponential decay, in particular in dendrites (reviewed extensivley in Jack, Noble, and Tsien, 1975). Softky (1994) derives an approximate expression for the peak potential and the rate of repolarization. By neglecting any leak conductances (that is, working in the limit of $R_m \rightarrow \infty$), the situation is formally equivalent to treating diffusion of charge inside a cylinder (see Fig. 11.3). This allows Softky to find the following expression for the peak depolarization in response to a very fast current pulse,

$$V_{\text{peak}} \approx 1.5 \frac{R_i^{1/2} I_{\text{peak}}}{(\pi d)^{3/2} C_m^{1/2}} \sqrt{t_{\text{peak}}}, \tag{3.57}$$

(see also Eq. 3.56). Note that R_m never appears here and that the peak potential scales with the square root of t_{peak}. Softky quantifies the rate of repolarization by estimating the time $\tau_{1/2}$ it takes for the potential to decay from V_{peak} halfway to zero,

$$\tau_{1/2} \approx 6 t_{\text{peak}}. \tag{3.58}$$

Figure 3.16 illustrates how well this approximation works for very rapid current inputs. It does badly on the slower components of the voltage decay since it completely neglects the effect of the membrane resistance.

As enthusiastically argued by Softky (1994, 1995), such rapid membrane dynamics, outpacing τ_m by far, give rise to the possibility of submillisecond coincidence detection in the thin basal and apical dendrites, in particular if Hodgkin-Huxley-like nonlinearities are present. We will pick up this story in Chap. 19.

3.7 Recapitulation

While Chap. 2 is concerned with solutions to the cable equation in single cables, this one concentrates on studying the membrane potential in realistic dendritic trees with the aim of understanding the relationship between dendritic architecture and function. A number of exact, recursive techniques exist to derive the membrane potential at any point in the dendritic tree in response to an arbitrary current injection at some other point. Because these techniques do not generalize well to n simultaneous inputs and do not work in the presence of membrane nonlinearities, today's method of choice is the numerical solution of the appropriately spatio-temporal discretized cable equation (compartmental method). Several well-documented, graphics-oriented, public software packages are available that implement the appropriate algorithms.

An alternative approach for gaining intuition about the events occurring in a dendritic tree is to "observe" the system at two points i and j, where the input is applied at i and the output recorded at j. The entire system can then be characterized in terms of three frequency-dependent functions that, in general, take on complex values: the input impedances $\tilde{K}_{ii}(f)$ and $\tilde{K}_{jj}(f)$ and the transfer impedance $\tilde{K}_{ij}(f) = \tilde{K}_{ji}(f)$. For sustained current input, these reduce to three real numbers, corresponding to the conventional input resistances $\tilde{K}_{ii}$

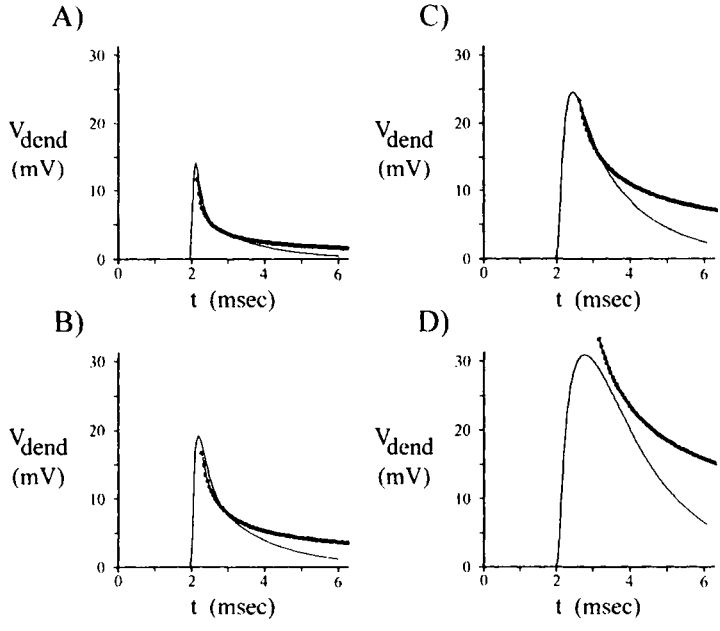

Fig. 3.16 Submillisecond Rise and Decay of Potentials Rapid membrane depolarization at the center of a thin basal dendrite of the pyramidal cell (close to *b*1 in Fig. 3.7) in response to local current injections with different rise times. The current took the form of Eq. 3.50 with t_{peak} of **(A)** 0.05, **(B)** 0.1, **(C)** 0.2, and **(D)** 0.4 msec. The approximations derived by Softky (1994) are indicated in bold. They describe well the peak membrane potential (Eq. 3.57) and the early part of the rapid repolarization. It is only during the slow, late part of the membrane depolarization, where the approximation diverges from the correct solution, that the membrane resistance plays any role. The somatic depolarizations in response to these inputs are minute, typically less than 0.5 mV. The morale is that brief and rapid synaptic inputs can give rise to changes in the membrane potential in the submillisecond range. Reprinted in modified form by permission from Softky (1994).

and $\tilde{K}_{jj}$ and transfer resistance $\tilde{K}_{ij}$ (with the dimensions of a resistance). This approach allows us to define in a straightforward manner the voltage attenuation $\tilde{A}_{is}$ between any dendritic site i and the soma s and the outgoing voltage attenuation $\tilde{A}_{si}$ from the soma to sites in the dendritic tree. This last measure is identical to the charge attenuation, the ratio of the total charge injected at the synaptic site i to the total charge reaching the soma.

The chapter also introduces the logarithmic transform of the attenuation, $\tilde{L}^{v}_{ij} = \ln |\tilde{A}_{ij}|$. As compared to a true distance metric, this measure is not symmetric: the logarithm of the voltage attenuation between i and j is different from the logarithm of the voltage decrement between j and i. Indeed, for passive trees, the voltage attenuation from any dendritic site to the soma is always considerably larger than in the reverse direction. The reason for this profound asymmetry is that dendritic sites have high impedance while the cell body has a low impedance. A further consequence is that, if integrated over sufficiently long times (in practice several time constants), about half of the total charge injected into distal dendritic sites can reach the soma. We discussed a frequently used measure of synaptic efficiency, the total electrotonic distance L_{is}. Due to the fact that real trees are quite distinct from infinite cables, this measure sharply underestimates the true voltage attenuation. All of this can be visualized graphically, using the morphoelectrotonic transforms. METs are a useful dynamic tool for portraying different features of the electroanatomy of a cell.

We also considered delays in the dendritic tree and between dendritic sites and the soma. Using the definition of delays in terms of differences in the centroids of voltages and currents, we can show that τ_m represents an upper bound on how slowly the voltage decays in response to fast inputs. At the soma, the local delay is on the order of the membrane time constant, while for distal sites the local delay can be much faster, as small as 5 or 10% of τ_m, implying that events in the dendritic tree can be very rapid. This is particularly true for rapid synaptic events in thin dendrites, where the rise and early decay times of the dendritic membrane potential are independent of R_m, allowing for the possibility of carrying out precise timing relationships in these structures that are not limited by τ_m.

The take-home message is that one has to be careful in applying the concepts that characterize an infinite cable (λ, τ_m, and R_{in}) to realistic neurons. These have finite arbors, with multiple dendrites terminating at different distances and branching patterns that do not obey the necessary geometrical constraints for reduction to an equivalent cylinder. These considerations have significant effects on how the voltage spreads and attenuates in dendrites and hence in how synaptic inputs are integrated.